AGU ADVANCING EARTH AND SPACE SCIENCES

AGU Advances

RESEARCH ARTICLE
10.1029/2023AV000972

Constitutive Behavior of Rocks During the Seismic Cycle

Sylvain Barbot[1]

[1]Department of Earth Sciences, University of Southern California, Los Angeles, CA, USA

Peer Review The peer review history for this article is available as a PDF in the Supporting Information.

Key Points:

- Frictional properties evolve with the thermal activation of competing healing and deformation mechanisms at different slip-rates
- A constitutive law explains gouge friction from room temperature to 600°C and slip-rates from nanometers to millimeters per second
- The frictional response during seismic cycles is controlled by lithology and the prevailing hydrothermal conditions

Supporting Information:

Supporting Information may be found in the online version of this article.

Correspondence to:

S. Barbot,
sbarbot@usc.edu

Citation:

Barbot, S. (2023). Constitutive behavior of rocks during the seismic cycle. *AGU Advances*, *4*, e2023AV000972. https://doi.org/10.1029/2023AV000972

Received 31 MAY 2023
Accepted 25 AUG 2023

Author Contributions:

Conceptualization: Sylvain Barbot
Data curation: Sylvain Barbot
Formal analysis: Sylvain Barbot
Funding acquisition: Sylvain Barbot
Investigation: Sylvain Barbot
Methodology: Sylvain Barbot
Project Administration: Sylvain Barbot
Resources: Sylvain Barbot
Software: Sylvain Barbot
Validation: Sylvain Barbot
Visualization: Sylvain Barbot
Writing – original draft: Sylvain Barbot

Abstract Establishing a constitutive law for fault friction is a crucial objective of earthquake science. However, the complex frictional behavior of natural and synthetic gouges in laboratory experiments eludes explanations. Here, we present a constitutive framework that elucidates the rate, state, and temperature dependence of fault friction under the relevant sliding velocities and temperatures of the brittle lithosphere during seismic cycles. The competition between healing mechanisms, such as viscoelastic collapse, pressure-solution creep, and crack sealing, explains the low-temperature stability transition from steady-state velocity-strengthening to velocity-weakening as a function of slip-rate and temperature. In addition, capturing the transition from cataclastic flow to semi-brittle creep accounts for the stabilization of fault slip at elevated temperatures. We calibrate the model using extensive laboratory data on synthetic albite and granite gouge, and on natural samples from the Alpine Fault and the Mugi Mélange in the Shimanto accretionary complex in Japan. The constitutive model consistently explains the evolving frictional response of fault gouge from room temperature to 600°C for sliding velocities ranging from nanometers to millimeters per second. The frictional response of faults can be uniquely determined by the in situ lithology and the prevailing hydrothermal conditions.

Plain Language Summary The frictional behavior of rocks is essential to understand fault activity and seismic unrest. Despite decades of research, the frictional behavior of rocks remains elusive. Although empirical parameters can be used to characterize the frictional behavior of fault gouge, they cannot consistently capture the evolution of frictional properties with temperature and sliding velocity. This is a theoretical bottleneck to earthquake forecasting. In this article, we present a physical model that explains the complex frictional response of various types of rocks from room temperature to 600°C within five orders of magnitude of sliding velocities. The model captures the dominance of distinct healing mechanisms at different ranges of temperature and the transition to crystal plasticity in the fault zone at elevated temperatures. As a result, a single set of constitutive parameters can explain the frictional response of rocks throughout the seismic cycle from the Earth's surface to the bottom of the lithosphere.

1. Introduction

The frictional properties of rocks play a crucial role in fault behavior and control a wide range of phenomena, from slow-slip events and tremors to the nucleation and propagation of earthquakes (e.g., Cebry et al., 2022; Conrad et al., 2023; Leeman et al., 2016; Tal et al., 2020). The rupture propagation style, source properties, and recurrence patterns of earthquakes are determined predominantly by the rheological properties of faults (Kaneko et al., 2010; Liang et al., 2022; Liu et al., 2012; Michel et al., 2017; Qiu et al., 2016; Veedu & Barbot, 2016). In principle, constitutive friction laws calibrated to experimental data provide an effective means of scaling up laboratory results to realistic crustal conditions and form the foundation of numerical simulations of fault dynamics, explaining natural observations or predicting new fault behaviors (e.g., Barbot, 2019a; Gauriau et al., 2023; Lapusta et al., 2000; Liu & Rice, 2005; Rice & Ruina, 1983; Ruina, 1983; Q. Shi et al., 2020; P. Shi et al., 2022; Tse & Rice, 1986; Zhu et al., 2020). Despite decades of laboratory and theoretical studies, the frictional behavior of rocks remains poorly understood. Although empirical formulations can reproduce laboratory data within a narrow range of conditions, a physical model is still missing, preventing extrapolation to natural conditions. This critical knowledge gap hinders the development of physics-based earthquake forecasting.

Realistic constitutive models of fault friction must reconcile many puzzling observations. The frictional resistance seems only weakly dependent on rock type and material hardness (Bowden & Tabor, 1950, 1964; Byerlee, 1978). In addition, the textural evolution of fault gouge or the surface of bare contact results in distinct direct and steady-state responses to perturbations and produces time-dependent healing at stationary contact (Dieterich, 1972, 1978, 1979, 1981; Engelder & Scholz, 1976; Linker & Dieterich, 1992; Scholz & Engelder, 1976).

Writing – review & editing: Sylvain Barbot

The ambient hydrothermal conditions have a major effect on frictional behavior (Blanpied et al., 1995, 1998; Nakatani, 2001). Although the frictional strength at steady-state is only weakly dependent on temperature (e.g., Stesky, 1978a; Lockner et al., 1986), dynamic changes in temperature induce a direct effect and an evolutionary response (Chester, 1994, 1995; Chester & Higgs, 1992; Coble et al., 2014; Higgs, 1981). When shear heating becomes significant, thermally activated reactions lubricate the fault interface, resulting in enhanced weakening (Acosta et al., 2018; Brantut et al., 2016; Brown & Fialko, 2012; Cornelio et al., 2019; Di Toro et al., 2006; Pozzi et al., 2019; Rowe et al., 2019; Tsutsumi & Shimamoto, 1997).

Understanding the frictional properties of rocks is crucial for predicting seismic activity and fault dynamics (Barbot et al., 2012; T. Chen & Lapusta, 2009; Kaneko et al., 2016; Lapusta & Rice, 2003; Nie & Barbot, 2022; Sathiakumar & Barbot, 2021; Veedu & Barbot, 2016; Veedu et al., 2020; B. Wang & Barbot, 2023). Empirical parameters can be used to characterize the frictional resistance, with constant values being desirable for realistic constitutive models. However, the evolution of frictional properties with temperature (An et al., 2020; den Hartog et al., 2012, 2021; Liu & He, 2020; Mitchell et al., 2016; Pec et al., 2016; Tian & He, 2019; Valdez et al., 2019; Yasuhara et al., 2005) and sliding velocity (Boulton et al., 2018; Carpenter, Collettini, et al., 2016; Collettini et al., 2011, 2019; den Hartog et al., 2012; Dieterich, 1978; Haines et al., 2014; Ikari & Kopf, 2017; Ikari & Saffer, 2011; Ikari, Ito, et al., 2015; Ikari, Trütner, et al., 2015; Kaproth & Marone, 2013; Kilgore et al., 1993; Lockner et al., 2011; Moore et al., 2016; Niemeijer & Collettini, 2014; Pec et al., 2016; Verberne et al., 2014) continues to elude explanation.

While the temperature control on the frictional behavior of pyroxene (Tian & He, 2019), amphibole (Liu & He, 2020), granite (Mitchell et al., 2016), smectite and illite (Kubo & Katayama, 2015), shale (An et al., 2020), and fault gouges (Boulton et al., 2014; den Hartog et al., 2021; Valdez et al., 2019) can be described by the competition between thermally activated healing mechanisms (Barbot, 2022), other rocks exhibit a more complex behavior. Albite (Nakatani, 2001) and Westerly granite (Blanpied et al., 1995, 1998) exhibit an increase in the direct effect parameter that cannot be explained with competing mechanisms of time-dependent healing (Figure 1). Interestingly, for Westerly granite gouge, this change is coincident with a transition from steady-state temperature-hardening to temperature-weakening, indicating a change in the underlying mechanism of deformation. Inspection of the sheared gouges in thin section reveals a transition from slip on oblique Riedel shear zones that pervade the gouge to localized strain along extremely comminuted, fault-parallel shear bands (Blanpied et al., 1995). Natural gouges from the Alpine Fault (Niemeijer et al., 2016) showcase distinct steady-state velocity-weakening and velocity-strengthening regimes controlled by temperature and sliding velocity (Figure 2). All samples show a transition from velocity-strengthening to velocity-weakening behavior with increasing temperature and decreasing velocity, but a second transition to velocity-strengthening friction occurs at even higher temperatures for sliding velocities lower than 100 μm/s. A similar frictional behavior is observed for metapelite (den Hartog et al., 2012) and basalt gouge (Okuda et al., 2023). A constitutive framework capturing the frictional resistance of these rocks under various temperatures and sliding velocities using constant coefficients is still needed.

Here, we present a constitutive framework that elucidates the slip-rate, state, and temperature dependence of fault friction for various lithology from room temperature to 600°C and sliding velocities ranging from nanometer to millimeter per second. In Section 2, we describe the modeling assumptions leading to the constitutive formulation. The competition between thermally activated healing mechanisms explains the evolution of friction at low temperatures, as in previous work (Barbot, 2022), but also captures the dependence on slip-rate. The additional competition between cataclasis and crystal plasticity explains the stabilization of slip at higher temperatures and lower slip-rates. In Section 3, we provide calculations that illustrate the relative contributions of competing healing and deformation mechanisms on the frictional behavior. In Section 4, we calibrate the model to laboratory data for synthetic albite (Nakatani, 2001) and granite gouge (Blanpied et al., 1995, 1998), and on natural samples from the Alpine Fault (Niemeijer et al., 2016) and the Mugi Mélange in the Shimanto accretionary complex (Okuda et al., 2023). More theoretical results are provided in Appendices A–C. As the constitutive law consistently captures the frictional behavior of rocks as a function of temperature and sliding velocity, the frictional response of faults may be uniquely determined by the in situ lithology and the prevailing hydrothermal conditions.

2. Constitutive Framework for Fault Friction

A constitutive model of fault friction must capture the direct dependence of sliding velocity on stress, state, and temperature and the evolutionary response to perturbations. In the brittle field, the state evolution is fundamentally linked to changes in the real area of contact (Ben-David & Fineberg, 2011; Ben-David et al., 2010; Dieterich & Kilgore, 1994; Rubinstein et al., 2004; Selvadurai & Glaser, 2015, 2017) with the strength of contact modulated by

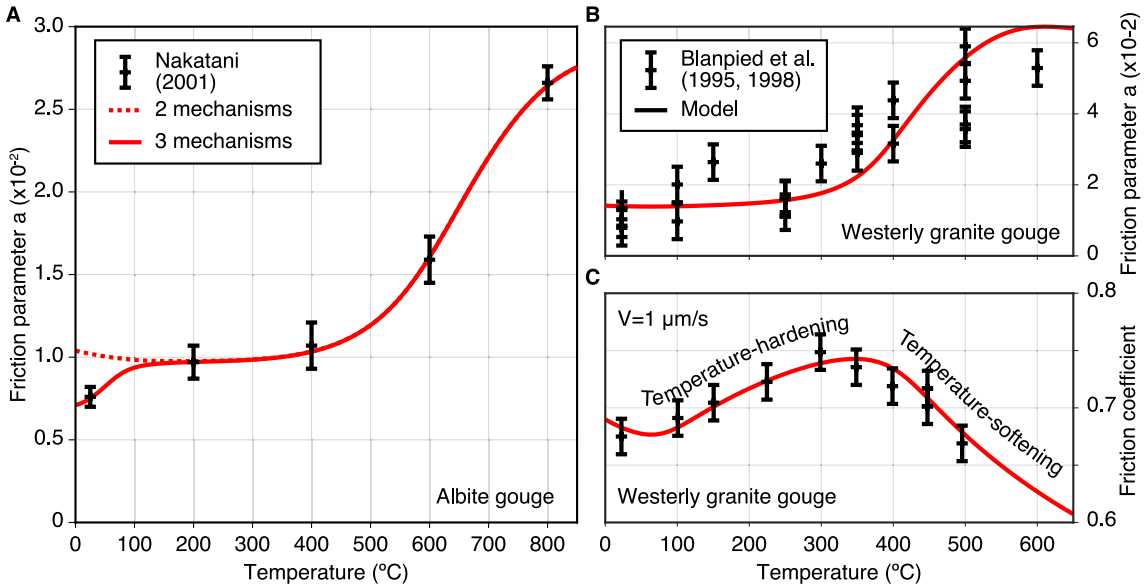

Figure 1. Temperature dependence of the direct effect frictional parameter a and the friction coefficient for albite and granitic gouge. (a) Temperature dependence of the direct effect parameter a for albite gouge (red error bars) (Nakatani, 2001). The models assume two (dashed line) and three (solid line) deformation mechanisms across the fault gouge. (b) Temperature dependence of the direct effect parameter (red error bars) for Westerly granite gouge in wet conditions (Blanpied et al., 1995, 1998). (c) Temperature dependence of the steady-state friction coefficient (red error bars) for Westerly granite gouge at a sliding velocity of 1 μm/s (Blanpied et al., 1995, 1998). The physical models (black lines) are presented in Section 4 and the assumed model parameters can be found in Table 2.

chemical reactions near contact junctions and crack tips in aqueous solutions or atmospheric humidity (Bergsaker et al., 2016; Dieterich & Conrad, 1984; Frye & Marone, 2002; Renard et al., 2012; Rostom et al., 2013; Zeng et al., 2020). The physical basis of the model relies on quantifying the real area of contact, which varies instantaneously with shear and normal stress, but also evolves spontaneously over time (Dieterich & Kilgore, 1994, 1996; Maegawa et al., 2015; Mergel et al., 2019; Popov et al., 2021; Sahli et al., 2018; Weber et al., 2019; Xu et al., 2022). In this study, we consider a simple model whereby the area of contact is controlled by the effective normal stress and the local radius of curvature of micro-asperities at contact junctions based on the roughness of natural surfaces with a fractal topography (Archard, 1957; Barbot, 2019b; Greenwood & Williamson, 1966)

$$\mathcal{A} = \frac{c_0 + \mu_0 \bar{\sigma}}{\chi} \left(\frac{d}{d_0} \right)^{\alpha}, \tag{1}$$

where $\mathcal{A}$ is the density of real area of contact, c_0 is a cohesion term, μ_0 is the reference friction coefficient, $\bar{\sigma}$ is the effective normal stress accounting for pore fluid pressure (Terzaghi, 1936), χ is the plowing hardness, d and d_0 are the effective and reference radii of curvature at contact junctions, and α is a power exponent. The expression $c_0 + \mu_0 \bar{\sigma}$ in the numerator can be thought of as the truncated Taylor series expansion of a more general expression that accounts for saturation of the area of contact at high effective stress and other effects at low confining pressure (e.g., Leu, 2009). However, as the indentation hardness of common rocks is of the order of gigapascals, the saturation of the real area of contact is expected at confining pressures beyond the brittle-ductile transition, where deformation is controlled by semi-brittle and ductile processes. Therefore, the linear form is widely applicable in the brittle field. As we assume $\alpha \ll 1$, the geometry of contact junctions is a second-order effect. The hardness for plowing and for indentation are related by the relation $\chi = \mu_0 \chi_n$ compatible with adhesion theory (Bowden & Tabor, 1950, 1964). We further assume that the real area of contact controls the yield strength, following

$$\sigma_Y = \mathcal{A} \chi. \tag{2}$$

These assumptions elucidate the origin of the Coulomb failure criterion (Coulomb, 1821) as combining Equations 1 and 2 and considering only the first-order term gives rise to $\sigma_Y = c_0 + \mu_0 \bar{\sigma}$, a widely used rate-independent condition for material failure. However, for the constitutive framework to enable seismic cycles, it must incorporate a rate dependence.

The velocity of fault-parallel sliding can be accommodated by cataclasis and crystal plasticity depending on temperature and slip-rate, each associated with a distinct stress sensitivity, grain-size dependence, and activation

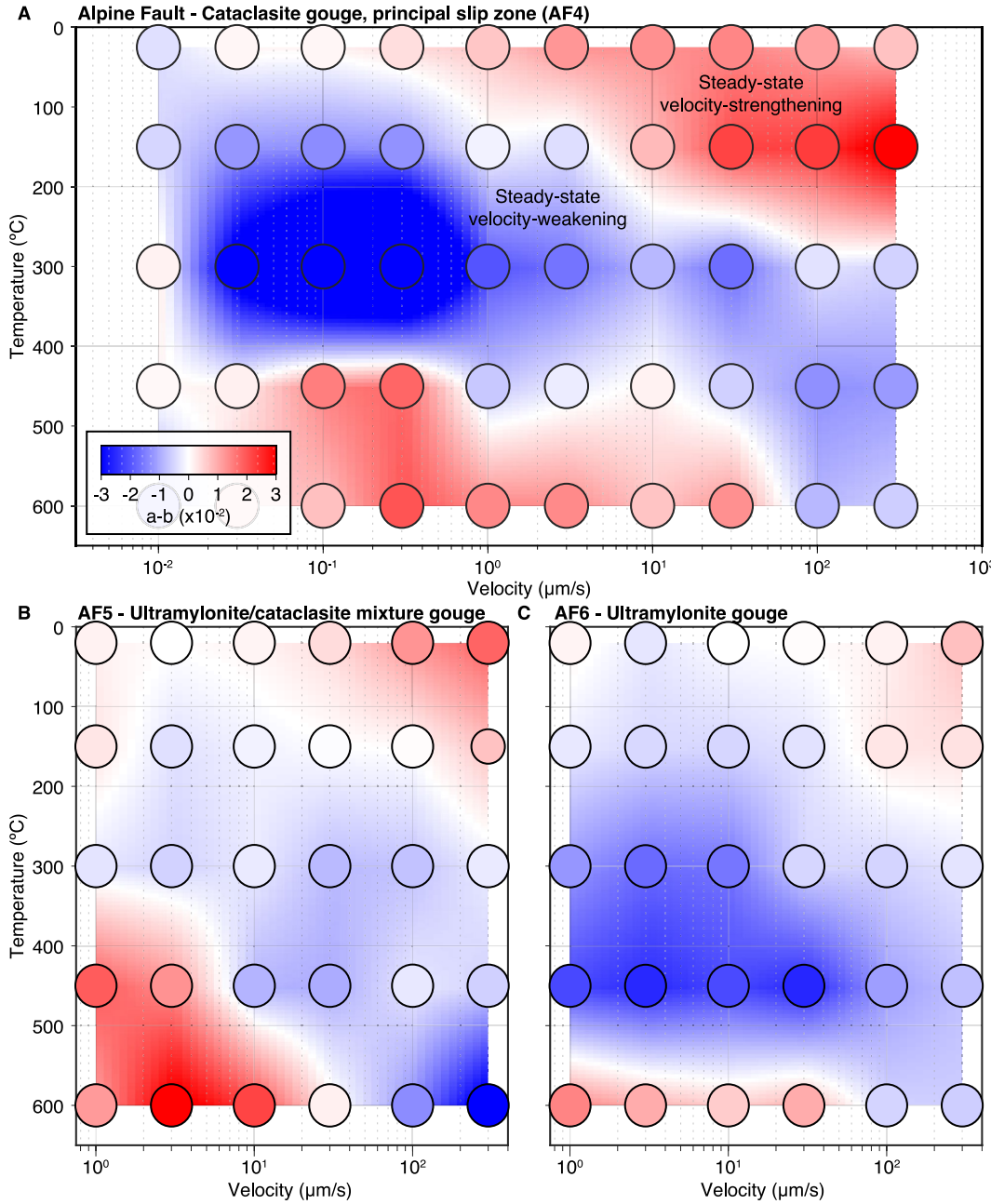

Figure 2. Steady-state velocity dependence of friction for natural samples from the Alpine Fault, New Zealand, obtained from the Deep Fault Drilling Project, as a function of temperature and velocity (Niemeijer et al., 2016). (a) Steady-state velocity-dependence parameter $a - b$ for cataclasite gouge sample AF4 from the principal slip zone from room temperature to 600°C and for slip-rates from nanometers to millimeters per second. (b) Same for ultramylonite gouge sample AF5 for slip-rates from 1 to 300 µm/s. (c) Same for ultramylonite gouge sample AF6. Steady-state velocity-weakening appears in blue and velocity-strengthening in red. The gouges exhibit three frictional domains of velocity-weakening (blue) and velocity-strengthening (red) steady-state friction. The background color is an interpolation of the experimental data (circles) obtained at discrete temperatures and slip-rates.

energy (e.g., Blanpied et al., 1995; Chester, 1995; Pec et al., 2016; Stesky, 1978a). Cataclastic flow involves pervasive gouge deformation mobilizing several mechanisms contributing at different rates, including granular flow, fracturing, and comminution. Granular flow proceeds by grain rotation, sliding, and neighbor swapping (J. Chen et al., 2017; Chevoir et al., 2009; MiDi, 2004). Deformation by fracturing occurs at the scale of individual grains and along millimeter-scale antithetic Riedel fractures formed by concentrated comminution that align

parallel or oblique to the direction of slip (Davis et al., 2000; He et al., 2006, 2007, 2013, 2016; Liu & He, 2020; Lu and He, 2014, 2018; Okuda et al., 2023; Riedel, 1929; Tian & He, 2019). In practice, fault gouge typically engages simultaneous fracturing, granular flow, and comminution in various proportions across the shear zone. Crystal plasticity localizes in narrow shear zones and involves intra-granular deformation, such as diffusion creep, grain-boundary sliding, dislocation creep, and Peierls creep, each associated with different power exponents and activation energies (Frost & Ashby, 1982; Karato, 2008; Poirier, 1985). Unlike brittle processes, ductile creep is weakly sensitive to normal stress, yet sensitive to grain size, as for example, in pressure-solution creep and grain-boundary sliding (Bürgmann & Dresen, 2008; Gratier et al., 2009; Hansen et al., 2011). The combined effect of these various vehicles for shearing of the fault gouge can be captured by the following constitutive relationship

$$\frac{V}{V_0} = \sum_{k=1}^{P} \left(\frac{\tau}{\sigma_Y}\right)^{n_k} \exp\left[-\frac{Q_k}{R}\left(\frac{1}{T} - \frac{1}{\bar{T}_k}\right)\right] + \sum_{k=P+1}^{M} \left(\frac{\tau}{\tau_0}\right)^{n_k} \left(\frac{d}{d_0}\right)^{-m_k} \exp\left[-\frac{Q_k}{R}\left(\frac{1}{T} - \frac{1}{\bar{T}_k}\right)\right], \tag{3}$$

that combines P brittle processes and $M - P$ ductile processes, where V and V_0 are the instantaneous and reference sliding velocities, τ, σ_Y, and τ_0 represent the norm of the shear traction, the yield strength in the brittle field, and a reference shear stress in the ductile regime, respectively, the n_k are power-law exponents, and the Q_k and $\bar{T}_k$ are the molar energies and temperatures of activation, respectively, with the universal gas constant R. The exponential terms in Equation 3 correspond to Arrhenius activation and the stress-dependent prefactor converts the frequency of success of the transformation to a slip velocity. The instantaneous velocity results from the integration of the plastic strain-rate across the gouge of thickness h and Equation 3 relates to the norm of the velocity vector. The model does not describe further localization within the gouge. The remaining assumption is that the velocity and traction vectors are co-aligned. The strain-rates are additive and the resulting velocity is summed over the M mechanisms of fault-parallel slip. For simplicity, we ignore the so-called transient creep that leads to strain hardening during an evolutionary phase in the ductile regime, although its effect on mechanical strength is well understood (Barbot, 2018, 2020a; Masuti & Barbot, 2021; Masuti et al., 2016; Sherburn et al., 2011; Tang et al., 2019, 2020). In the following, we order the mechanisms by increasing activation energy, such that $Q_k \leq Q_{k+1}$ for any k.

A unified rate-, state-, and temperature-dependent friction law with multiple deformation mechanisms that reconciles the above considerations can be written as follows

$$V = \sum_{k=1}^{M} V_0 \left(\frac{\tau}{c_k + \mu_k \bar{\sigma}}\right)^{n_k} \left(\frac{d}{d_0}\right)^{-m_k} \exp\left[-\frac{Q_k}{R}\left(\frac{1}{T} - \frac{1}{\bar{T}_k}\right)\right], \tag{4}$$

where $m_k = \alpha n_k$ for brittle processes and $\mu_k = 0$ for ductile processes. For purely rate-dependent creep, $m_k = 0$ and the curvature of micro-asperities does not affect strength. The slip velocity can be directly inferred given the shear and normal stress, temperature, and size of micro-asperities. The shear stress can exceed the yield strength, simply producing elevated slip-rate in that case. Reciprocally, sliding also occurs below the yield strength, but at vanishing rates. The first deformation mechanism is associated with six independent constitutive parameters, as V_0, d_0, and $\bar{T}_1$ trade off with each other. However, the addition of deformation mechanisms requires merely three new parameters (n_k, Q_k, and $\bar{T}_k$) per mechanism. Given the multiplicative form of the flow law of Equation 4, the rate, state, and temperature dependence of friction can be characterized by the phenomenological parameters

$$n = \frac{\partial \ln V}{\partial \ln \tau}, \qquad m = \frac{\partial \ln V}{\partial \ln d}, \tag{5}$$

and

$$Q = \frac{-\partial \ln V}{\partial (1/RT)}, \tag{6}$$

which may not be constant. The effective power-law exponent and activation energy vary with rock type and temperature, typically falling within the range of $n = 10$–170 and $Q = 10$–150 kJ/mol in the brittle field (Atkinson, 1984; Barbot, 2019b, 2022). In granitoid rocks, the exponent decreases from $n \approx 140$ at 300°C to $n \approx 10$ at 600°C with

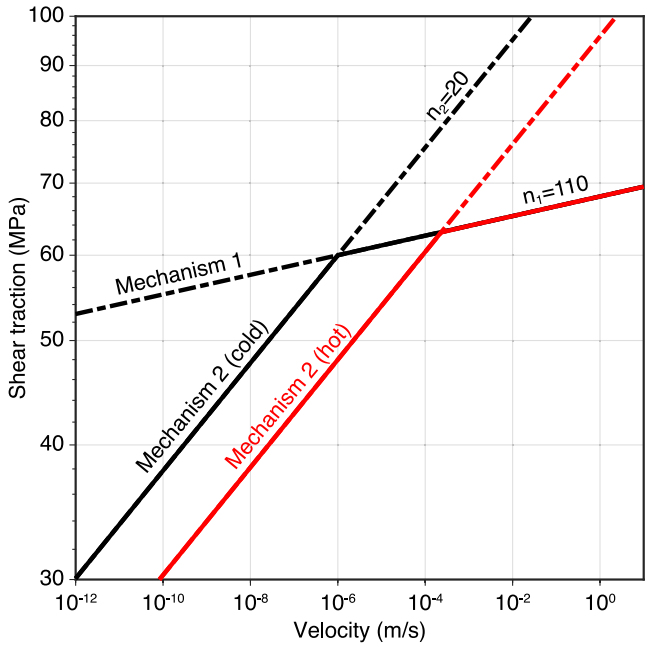

Figure 3. Schematic temperature and velocity dependence of the direct effect parameter. The competition between two mechanisms with different stress-velocity relationships (power-law exponent $n_1 = 110$ for the solid line and $n_2 = 20$ for the dashed line) gives rise to a velocity dependence of the direct effect parameter. The thermal activation of mechanism 2 increases the range of velocities in which it dominates, giving rise to a temperature and velocity dependence of the direct effect parameter.

the activation energy ranging from 80 ± 20 to 180 ± 50 kJ/mol depending on strain-rate (Pec et al., 2016). Incorporating multiple shear mechanisms with distinct stress sensitivity and activation energy provides a straightforward explanation for the velocity and temperature dependence of the direct effect (Figure 3). Different mechanisms will be activated depending on the sliding velocity, each associated with its own stress versus slip-rate relationship. In addition, the velocity at which the transition occurs will change depending on temperature. For multiple mechanisms to be useful to consider in practice, the parameters n_k and Q_k must be sufficiently distinct. Mechanisms characterized by similar constitutive parameters cannot be distinguished based on fault strength alone.

The last component of the constitutive model is the evolution of the real area of contact from the competition between time-dependent healing and contact rejuvenation during fault slip (Barbot, 2019b, 2022). Healing occurs by compaction creep, that is, time-dependent shortening of the gouge layer leading to an increase of the real area of contact, or by cementation of the fluid-filled cavities that pervade the gouge. Compaction creep takes place by a variety of micro-physical deformation processes that accommodate fault-perpendicular strain and is primarily driven by the effective normal stress, which induces local shear within the microstructure. In dry conditions, viscoelastic collapse of micro-asperities can occur by intra-granular flow, such as diffusion creep and dislocation creep (Frost & Ashby, 1982; Karato, 2008; Poirier, 1985) or comminution by subcritical crack growth (Bernabé & Pec, 2022; Charles, 1958; Rostom et al., 2013; Wiederhorn, 1967). In wet conditions, from atmospheric humidity to saturated pore space, plastic deformation of asperities can occur by pressure-solution creep (Cox & Paterson, 1991; Gratier et al., 2009; He et al., 2013; Kanagawa et al., 2000; Renard et al., 2000; Yasuhara et al., 2005), but the flattening of contact junctions can occur by the cementation of the pore space or crack tips (Tenthorey & Cox, 2006; Tenthorey et al., 2003; Wintsch et al., 1995). The rate of healing can also be affected by mineral composition (Hirauchi et al., 2023; A. H. Kohli & Zoback, 2013; Ruggieri et al., 2021; Shreedharan et al., 2022, 2023; F. Zhang et al., 2019).

The competition between N healing mechanisms acting on different minerals can be captured by an additive formulation that generalizes the aging law (Barbot, 2022)

$$\frac{\dot{d}}{d} = \sum_{k=1}^{N} \frac{G_k}{p_k d^{p_k}} \exp\left[-\frac{H_k}{R}\left(\frac{1}{T} - \frac{1}{T_k}\right)\right] - \frac{\lambda V}{2h}, \tag{7}$$

where each healing rate is characterized by the size-sensitivity power exponent p_k, the activity G_k, and the molar energy and temperature of activation H_k and T_k, respectively. The negative term corresponds to the weakening associated with contact rejuvenation for a plastic strain-rate $V/(2h)$, where h is the thickness of the gouge layer, given the characteristic strain for contact erosion $1/\lambda$. Equation 7 is compatible with a stress versus strain-rate relationship whereby the strain-rate is captured by $\dot{d}/d$ and the term $1/d^{p_k}$ represents a power-law of stress combined with a grain-size sensitivity. We order the mechanisms by increasing activation energy, such that $H_k < H_{k+1}$ for any k. As all the experiments considered herein are conducted in isobaric conditions, we ignore a possible dependence of healing rate to varying normal stress (Linker & Dieterich, 1992; Sleep, 2005, 2006). The evolution law can also be cast as a multiplicative formulation that generalizes the slip law (Barbot, 2022)

$$\frac{\dot{d}}{d} = \frac{\lambda V}{2h} \ln\left\{\frac{2h}{\lambda V} \sum_{k=1}^{N} \frac{G_k}{p_k d^{p_k}} \exp\left[-\frac{H_k}{R}\left(\frac{1}{T} - \frac{1}{T_k}\right)\right]\right\}, \tag{8}$$

where the rejuvenation rate divides the total healing rate. The additive and multiplicative forms exhibit different evolutionary phases upon perturbation but produce the same response at steady-state. Therefore, the evolutionary effects can be described by the empirical parameters

$$p = -\left.\frac{\partial \ln V}{\partial \ln d}\right|_{ss}$$
$$H = -\left.\frac{\partial \ln V}{\partial (1/RT)}\right|_{ss}, \tag{9}$$

using either Equation 7 or Equation 8, where "ss" refers to the steady-state condition defined as $\dot{d} = 0$. The competition between healing mechanisms, whether using the additive or multiplicative form, can explain the transition from steady-state velocity-strengthening at room temperature to velocity-weakening at higher temperatures observed in several types of gouges using $0.5 \leq p/m \leq 2.5$ and molar activation energies in the range $20 \leq H \leq 130$ kJ/mol (Barbot, 2022). The formulation is compatible with the low power exponent of ductile processes (Bürgmann & Dresen, 2008) and nanometric flow within the principal slip zone governed by quasi-linear sensitivity to stress with low activation energy (Sun & Pec, 2021). Equations 7 and 8 equally apply in the brittle and ductile regimes as micro-asperity size modulates the strength of contact junctions (Barbot, 2019b) and the strain-rate of plastic flow (Hall & Parmentier, 2003; Hirth & Kohlstedt, 2003).

In this study, we refer to a "deformation mechanism" as a means for slip in the fault-parallel direction, as used in Equations 3 and 4. A "healing mechanism" points to a process of time-dependent strengthening in the evolution laws of Equations 7 and 8. Healing can be accompanied by fault-perpendicular strain, that is, compaction creep, if accommodated by micro-asperity creep, sub-critical crack growth, or pressure-solution creep. However, other processes can strengthen the fault without strain, such as crack sealing and cementation of pore space. In most rocks, the low-temperature transition from velocity-strengthening to velocity-weakening at steady-state occurs with a drastic change of the evolutionary phase without discernible change in the direct effect, suggesting the independence of the healing and deformation mechanisms. With the constitutive framework defined, we can readily inspect the velocity and temperature dependence of shear stress at steady-state, which can be described by (Appendix A)

$$\left.\frac{\partial \ln \tau}{\partial \ln V}\right|_{ss} = \frac{1}{n}\left(1 - \frac{m}{p}\right)$$
$$\left.\frac{\partial \ln \tau}{\partial (1/RT)}\right|_{ss} = \frac{1}{n}\left(Q - \frac{m}{p}H\right). \tag{10}$$

The model becomes rate- and temperature-dependent at steady state, admitting velocity-strengthening for $m < p$, velocity-neutral for $m = p$, and velocity-weakening for $m > p$ as well as temperature-hardening for $Qp < mH$, temperature-neutral for $Qp = mH$, and temperature-weakening for $Qp > mH$. With brittle processes, we always have $m = \alpha n$ (Appendix A). Given the competition between thermally activated deformation mechanisms, n and Q may be complicated functions of velocity and temperature. The simultaneous competition between healing mechanisms makes p a separate function of temperature and velocity. As a result, the constitutive framework allows for different regimes of steady-state velocity and temperature dependence. In the following section, we present numerical simulations that illustrate the influence of competing healing and deformation mechanisms on the frictional properties of fault gouge.

3. Effect of Multiple Deformation and Healing Mechanisms

We now discuss some numerical simulations and analytic results that shed light on the constitutive behavior. In laboratory and theoretical studies, the direct and steady-state frictional responses are commonly described by the empirical parameters

$$a = \frac{\partial \mu}{\partial \ln V}$$
$$a - b = \frac{\partial \mu_{ss}}{\partial \ln V}, \tag{11}$$

respectively. The transition from steady-state velocity-strengthening at room temperature to velocity-weakening at higher temperatures can be explained by the competition between healing mechanisms (Barbot, 2022). To describe the joint effects of temperature and slip-rate on frictional stability, we simulate velocity-step experiments for a spring-slider assembly based on the constitutive framework described in Section 2. After sliding at steady-state at sliding velocity V_1, we impose a sudden jump to velocity $V_2 > V_1$ and simulate the evolutionary phase. We use the simulated time series of shear stress to estimate the direct and steady-state effects of velocity following Equation 11. The details of the procedure are described in Appendix B.

Table 1
Default Constitutive Parameters Used for the Simulations of Figures 4–6

Physical parameter	Symbol	Value
Reference friction	μ_0	0.74
Asperity size exponent	α	0.03
Reference velocity	V_0	1 μm/s
Reference curvature at contact junctions	d_0	1 μm
Reference temperature	$\bar{T}_0$	20°C
	$\bar{T}_1$	420°C
Stress exponent	n_1	100
	n_2	40
Activation energy	Q_1	50 kJ/mol
	Q_2	125 kJ/mol
Healing power exponent	p_1	6.6
	p_2	1.8
	p_3	4.5
Healing activation energy	H_1	25 kJ/mol
	H_2	45 kJ/mol
	H_3	350 kJ/mol
Healing reference temperature	T_1	20°C
	T_2	150°C
	T_3	250°C
Weakening reference strain	$1/\lambda$	5%
Shear zone thickness	h	0.5 mm

Note. The reference healing rate is always $G_k = (1\ \mu\text{m})^{p_k}/\text{s}$ for mechanism k. The power exponent for the size of micro-asperity is $m_k = \alpha n_k$. Certain parameters are ignored in simulations with fewer healing or deformation mechanisms. Deviations from these parameters are indicated in the text and figures.

We first consider two healing mechanisms with a single deformation mechanism. We use $\alpha = 0.03$, $n = 100$, $m_1 = \alpha n$, $p_1 = 6.6$, $p_2 = 1.8$ with the activation energies $H_1 = 25$ kJ/mol and $H_2 = 85$ kJ/mol and activation temperatures $T_1 = 0$°C and $T_2 = 150$°C. The remaining parameters are listed in Table 1. The resulting distribution of $a - b$ is shown in Figure 4a. The model features two frictional regimes with velocity-strengthening at room temperature transitioning to velocity-weakening at higher temperature or lower slip velocity. The distribution of $a - b$ is reminiscent of the experimental data for the Alpine Fault gouge for temperatures lower than 300°C (Figure 2). To illustrate the role of the thermodynamic properties, we conduct another simulation using a lower activation energy $H_2 = 45$ kJ/mol (Figure 4b). This produces a similar pattern, except that velocity-weakening is obtained at higher velocities, suggesting that laboratory data at low temperatures can be explained by adjusting the thermodynamic parameters.

If the competition between two healing mechanisms can explain the low-temperature stability transition, it is reasonable to speculate that adding another healing mechanism may explain the second transition to velocity-strengthening at higher temperatures. To test this hypothesis, we extend the previous model with a third healing mechanism characterized by $p_3 = 4.5$, $H_3 = 350$ kJ/mol, and $T_3 = 250$°C. The distribution of $a - b$ is shown in Figure 4c. The model now features three frictional regimes with a second transition to velocity-strengthening at higher temperatures, as expected. However, the velocity-weakening domain extends to high temperatures for sufficiently low sliding velocity, a pattern that goes firmly against the laboratory observations for temperatures above 300°C (Figure 2). To illustrate the role of thermodynamic parameters, we present another simulation with $H_3 = 450$°C (Figure 4d). The distribution of $a - b$ shows a similar pattern at high temperatures, except that velocity-weakening requires a lower velocity. Regardless of constitutive parameters, the model with three healing mechanisms predicts velocity-strengthening behavior with increasing velocity, in blatant contradiction with the mechanical data for the mylonitic and cataclastic gouges of the Alpine Fault (Figure 2). We can therefore reject the hypothesis that the high-temperature stability transition is caused by the activation of another healing mechanism.

We now show that the high-temperature transition to velocity-strengthening is caused by a change of deformation mechanism. We simulate velocity-jump experiments with a single healing mechanism characterized by $p_1 = 1.8$, $H_1 = 45$ kJ/mol, and $T_1 = 150$°C and two deformation mechanisms with $n_1 = 100$, $n_2 = 40$, $Q_1 = 50$ kJ/mol, $Q_2 = 150$ kJ/mol, $\bar{T}_1 = 20$°C, and $\bar{T}_2 = 380$°C. The corresponding distribution of $a - b$ is shown in Figure 5a. The model exhibits two frictional regimes with a transition from velocity-weakening at low temperatures to velocity-strengthening at high temperatures. The pattern is compatible with the laboratory observations for the Alpine Fault gouge above 300°C, whereby velocity-weakening is enhanced with increasing velocities at high temperatures. The transition occurs because the empirical parameters defined in Equation 11 are connected to the constitutive parameters of Section 2. Application of the chain rule with Equations 5 and 11 leads to

$$\begin{aligned} a &= \frac{\mu}{n} \\ a - b &= \frac{\mu}{n}\left(1 - \frac{m}{p}\right), \end{aligned} \tag{12}$$

with $m = \alpha n$ for brittle processes. Hence, the variations of n and p drive equivalent variations of a and $a - b$. When two or more deformation mechanisms are in force, n evolves gradually, leading to corresponding variations in a and $a - b$. We provide more insights on this relationship in Appendix A. To illustrate the expected distribution of the high-temperature velocity-strengthening domain, we conduct other numerical experiments varying the thermodynamic properties of the second deformation mechanism (Figures 5b–5d). Decreasing the power-exponent n_2 or the activation temperature $\bar{T}_2$ affects the amplitude of $a - b$ and the transition temperature.

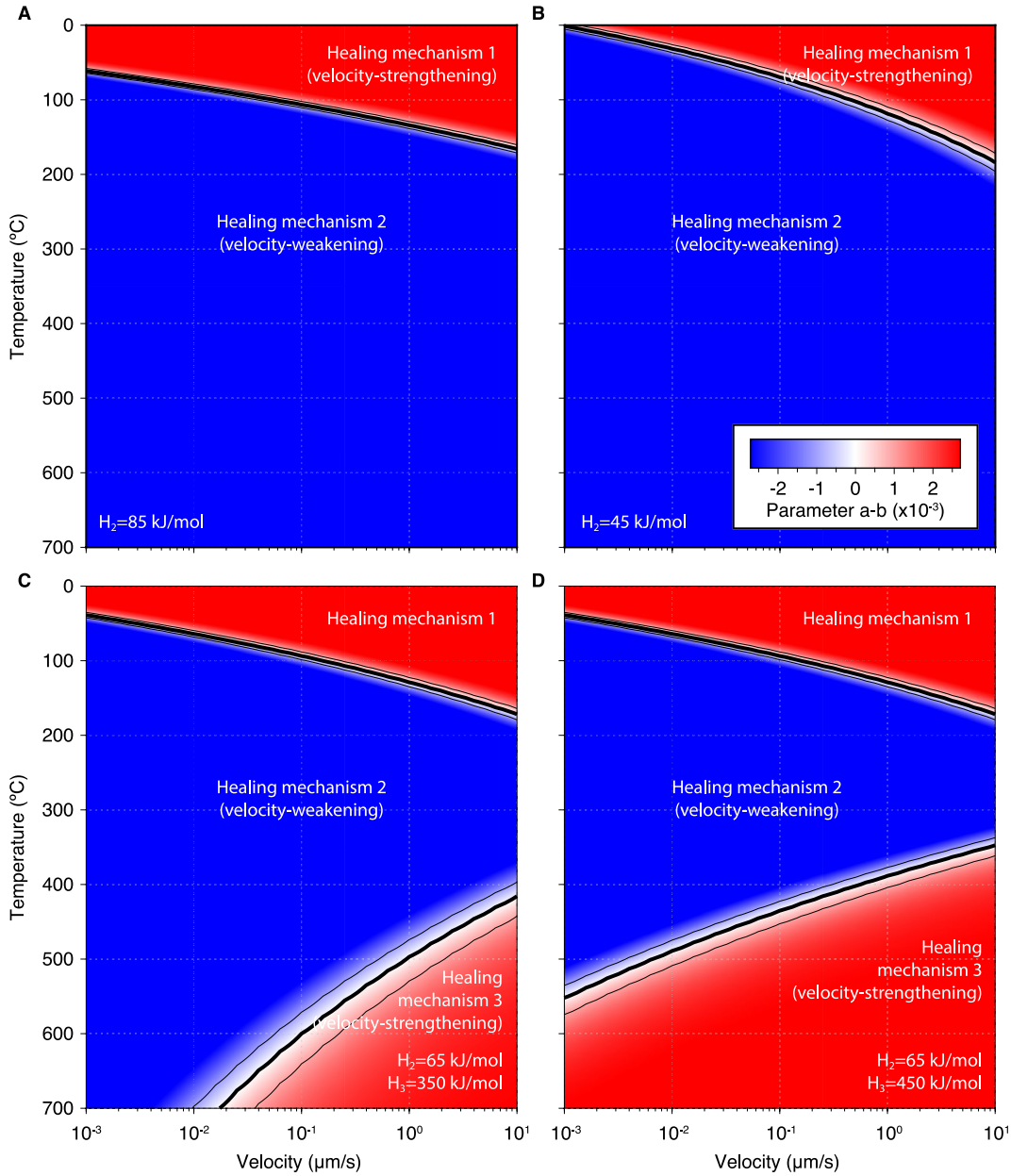

Figure 4. Effect of competing healing mechanisms on the temperature and velocity dependence of the steady-state velocity parameter. (a) Case of 2 competing healing mechanisms with $H_1 = 25$ kJ/mol and $H_2 = 85$ kJ/mol. (b) Case of 2 competing healing mechanisms with $H_1 = 25$ kJ/mol and $H_2 = 45$ kJ/mol. With two healing mechanisms, faults are velocity-weakening at steady-state for sufficiently high temperature. (c) Case of 3 competing healing mechanisms with $H_1 = 25$ kJ/mol, $H_2 = 65$ kJ/mol, and $H_3 = 350$ kJ/mol. (d) Case of 3 competing healing mechanisms with $H_1 = 25$ kJ/mol, $H_2 = 65$ kJ/mol, and $H_3 = 450$ kJ/mol. With three healing mechanisms, faults are steady-state velocity-weakening at sufficiently low sliding velocity.

Reducing the activation energy Q_2 reduces the velocity-strengthening domain. Within a realistic range, the thermodynamic parameters produce sufficient variability to calibrate the model against laboratory observations.

Producing a pattern of temperature and velocity dependence of $a - b$ compatible with the mechanical data for the Alpine Fault gouge requires a combination of two healing mechanisms and two deformation mechanisms. We illustrate the expected behavior with numerical simulations. The two deformation mechanisms are characterized by $\alpha = 0.03$, $n_1 = 100$, $n_2 = 33$, $\bar{T}_1 = 20°C$, $\bar{T}_2 = 420°C$, $Q_1 = 50$ kJ/mol, and $Q_2 = 150$ kJ/mol with $m_k = \alpha n_k$. The two healing mechanisms are associated with $p_1 = 6.6$, $p_2 = 1.8$, $H_1 = 25$ kJ/mol, $H_2 = 45$ kJ/mol, $T_1 = 0°C$,

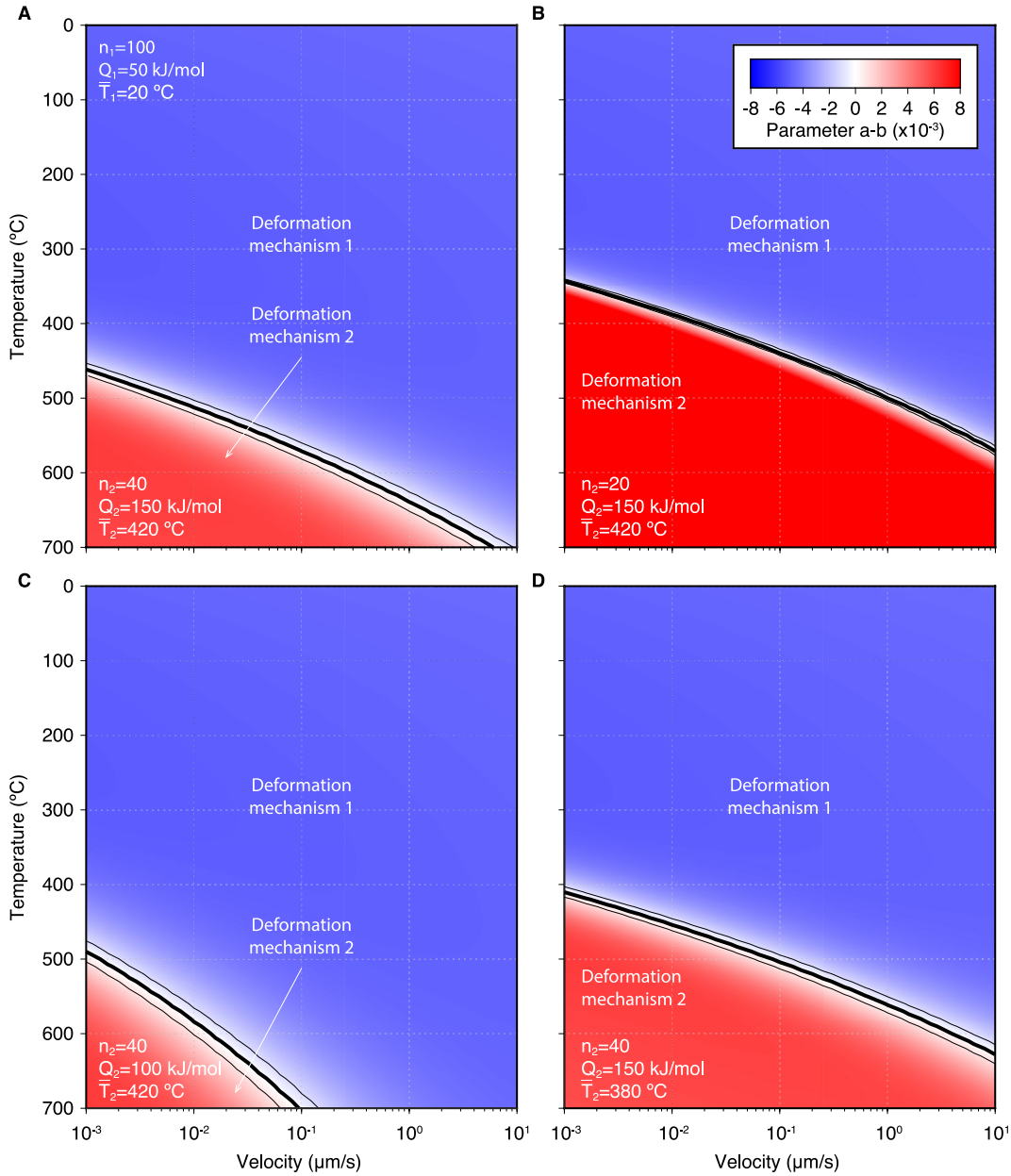

Figure 5. Effect of competing deformation mechanisms on the temperature and velocity dependence of the steady-state velocity parameter. (a) Case of two competing deformation mechanisms with $n_1 = 100$, $n_2 = 40$, $Q_1 = 50$ kJ/mol, $Q_2 = 150$ kJ/mol, $\bar{T}_1 = 20$°C, and $\bar{T}_2 = 420$°C. Panel (b) similar to (a), but with $n_2 = 20$. Panel (c) is similar to (a), but with $Q_2 = 100$ kJ/mol. Panel (d) is similar to (a), but with $\bar{T}_2 = 380$°C. The thermodynamic properties of the deformation mechanisms control the range of the velocity-strengthening domain at high temperatures.

and $T_2 = 250$°C. The corresponding distribution of a-b with temperature and velocity is shown in Figure 6a. The low-temperature transition occurs due to the competition between two healing mechanisms in a range of temperatures and slip-rates where a single deformation mechanism operates. The high-temperature transition takes place due to a change of deformation mechanism under the prevailing healing mechanism, leading to three frictional regimes, as observed in laboratory experiments (e.g., den Hartog et al., 2012; Niemeijer et al., 2016; Okuda et al., 2023).

We further describe the constitutive behavior with the detailed frictional response upon velocity steps at various temperatures and velocities (Figures 6c and 6d). The figures highlight the direct and evolutionary effects and detail the temperature and velocity dependence of a, b, and the characteristic weakening distance L. The effect

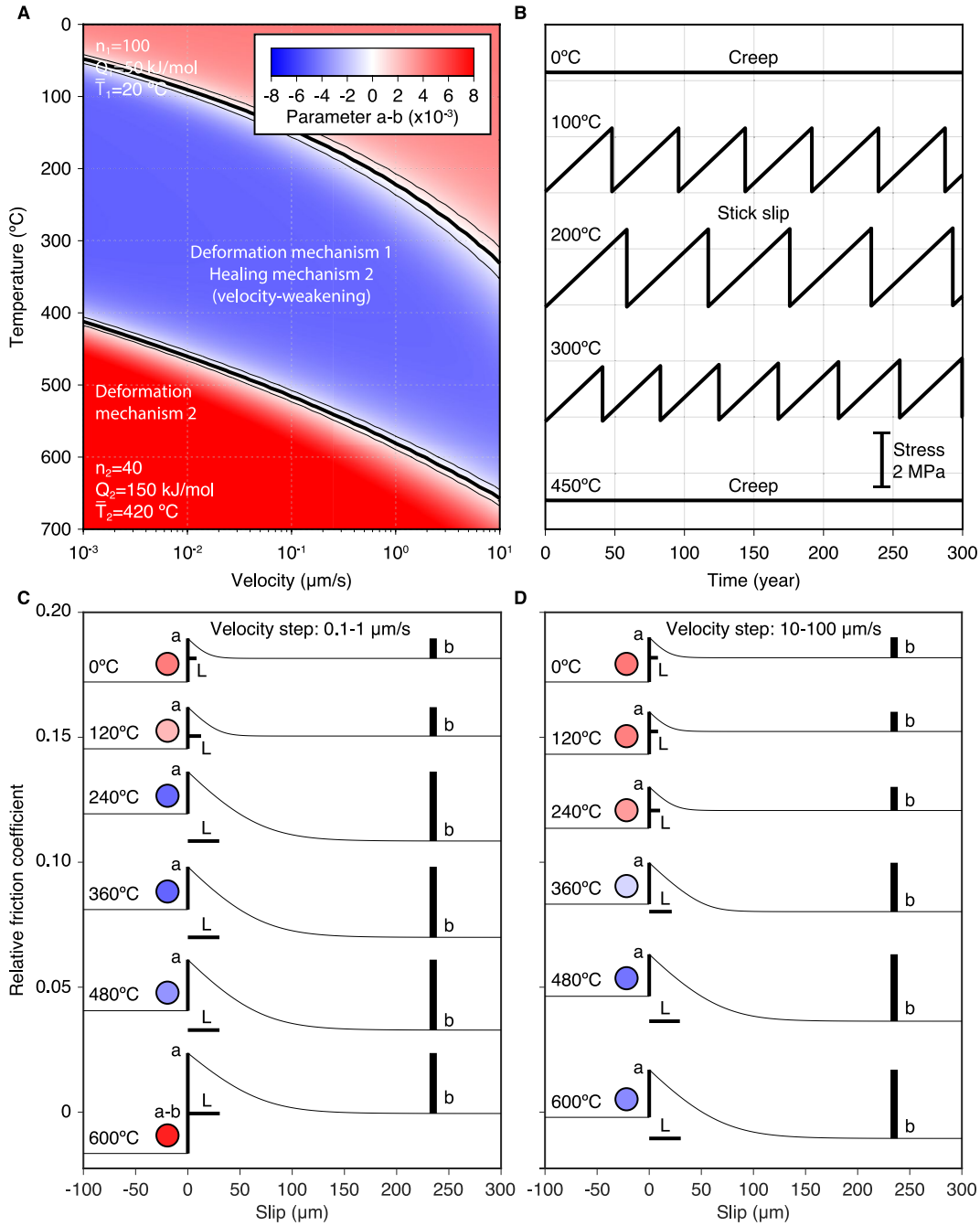

Figure 6. Effect of competing healing and deformation mechanisms on the frictional response of fault gouge. (a) Distribution of the steady-state velocity dependence parameter $a - b$ as a function of temperature and slip-rate showing three distinct frictional regimes. (b) Numerical simulations of creep and stick-slip in a spring-slider model loaded at a constant rate with the constitutive model described in Section 2 and the parameters used in the other plots. (c) Detailed frictional response upon imposed velocity steps from 0.1 to 1 μm/s with infinite stiffness. The variations of a and b are caused by transitions of deformation and healing mechanisms, respectively. The colored circles indicate the value of $a - b$ using the color scale in (a). The inferred values of a, b, and L are indicated by vertical and horizontal black bars. Panel (d) is the same for velocity steps from 10 to 100 μm/s. The constitutive parameters are described in the main text and listed in Table 1.

of ambient temperature for velocity steps from $V_1 = 0.1$ μm/s to $V_2 = 1$ μm/s is shown in Figure 6c. A sharp transition from steady-state velocity-strengthening to velocity-weakening occurs at 150°C due to an increase of b caused by the transition of healing mechanisms. This is accompanied by a minor change in the characteristic weakening distance. There is no substantial change in a up to 500°C. At 600°C, the direct effect parameter a

increases two-fold while b decreases slightly. This leads to a transition to steady-state velocity-strengthening. The effect of temperature for velocity steps from $V_1 = 10$ μm/s to $V_2 = 100$ μm/s is shown in Figure 6d. A similar transition from steady-state velocity-strengthening to velocity-weakening with increasing temperature occurs at 300°C due to the change of healing mechanism, but the second transition at high temperature does not take place. As the ambient frictional regime is velocity-weakening, it is enhanced at high velocity, moving the transition to even higher temperatures.

The constitutive framework predicts a velocity-weakening regime that operates at temperatures up to 650°C for sufficiently high velocities. However, in nature, frictional instabilities initiate at low sliding velocities of the order of 1 nm/s. At these velocities, the velocity-weakening regime is limited to a more narrow range of temperatures, from 50 to 400°C in this particular model. To better understand the frictional behavior during seismic cycles, we explore the stability of a spring-slider assembly upon a constant loading rate (Figure 6b). The method is described in Appendix C. The constitutive parameters are the same as for Figures 6a, 6c, and 6d. At room temperature, corresponding to a steady-state velocity-strengthening domain, we obtain persistent creep. From 100 to 400°C, within the steady-state velocity-weakening domain at low velocity, we obtain stick-slip events with variable stress drops. Finally, at 450°C, the system exhibits persistent creep again. As nucleation is prevented at these temperatures, the system never reaches the velocity-weakening regime found at higher velocities. In nature, ruptures may nucleate in a narrow range of temperatures, but eventually propagate to greater depths due to dynamic effects.

As the constitutive framework reproduces the broad patterns observed in laboratory experiments, we may explain the frictional properties of synthetic and natural gouges quantitatively by calibrating the thermodynamic and other constitutive parameters of the healing and deformation mechanisms.

4. Comparison With Laboratory Data

We now compare the model with observations from laboratory experiments. We first consider the constraints on the direct effect parameter of fine-powdered albite gouge (Nakatani, 2001). The experiments are conducted on a double-direct shear apparatus under constant normal stress of 20 MPa without pore water. Slide-hold-slide experiments are used to estimate the direct effect parameter a from room temperature to 800°C. The analysis of experimental data provides $a = 0.0075$, 0.0096, 0.0107, 0.0162, and 0.0261, for temperatures of 25, 200, 400, 600, and 800°C, respectively (Figure 1a). The bulk of the measurements can be explained by the competition between $P = M = 2$ brittle deformation mechanisms characterized by $n_1 = 75$, $n_2 = 23$, $Q_1 = 50$ kJ/mol, $Q_2 = 65$ kJ/mol, $\bar{T}_1 = 20$°C, and $\bar{T}_2 = 290$°C (dashed line in Figure 1a). The other parameters have little influence on the results and are essentially unconstrained with these data alone. The model captures the step-wise transition from $a \approx 0.01$ between 100 and 500°C to a more than two-fold increase at 800°C. However, the model slightly over-predicts the direct effect at room temperature. Invoking three mechanisms, for example, with a predominance of granular flow at room temperature, with $n_1 = 110$, $n_2 = 75$, $n_3 = 23$, $Q_1 = 20$ kJ/mol, $Q_2 = 50$ kJ/mol, $Q_3 = 65$ kJ/mol, $\bar{T}_1 = 0$°C, $\bar{T}_2 = 20$°C, and $\bar{T}_3 = 290$°C (solid black line in Figure 1a) allows us to tightly fit all the observations. However, with the available data for dry albite powder, the other model parameters are poorly constrained and many different combinations can fit the laboratory observations within uncertainties.

We now focus on the frictional response of Westerly granite gouge in wet conditions (Blanpied et al., 1995, 1998). The experimental procedure consists of velocity steps ranging from 0.01 to 1 μm/s at temperatures from 23 to 600°C under 400 MPa of effective normal stress accounting for 100 MPa of pore-fluid pressure. The frictional response exhibits complex variations of the friction coefficient, the direct and steady-state parameters, and the characteristic weakening distance with temperature and velocity (Figure 7). The mechanical results delineate two deformation regimes. Below 250°C, the coefficient of friction is high (0.7–0.8) and depends weakly on temperature and a transition from steady-state velocity-strengthening to velocity-weakening occurs at about 100°C. The transition to the second regime occurs at 350°C, above which the steady-state frictional response is substantially temperature-weakening and velocity-strengthening. The frictional properties can be explained with the proposed constitutive framework invoking two healing mechanisms and two deformation mechanisms, as explained in Section 3. Analysis of the sheared gouge in thin section identifies the deformation mechanisms as cataclastic flow, characterized by pervasive shear, Riedel fractures, and grain-size reduction across the gouge, and localized flow by crystal plasticity in narrow shear bands (Blanpied et al., 1995).

To explain the mechanical data on wet granite gouge quantitatively, we optimize the constitutive parameters by grid search. We consider $P = M = 2$ deformation mechanisms and $N = 2$ healing mechanisms. We obtain

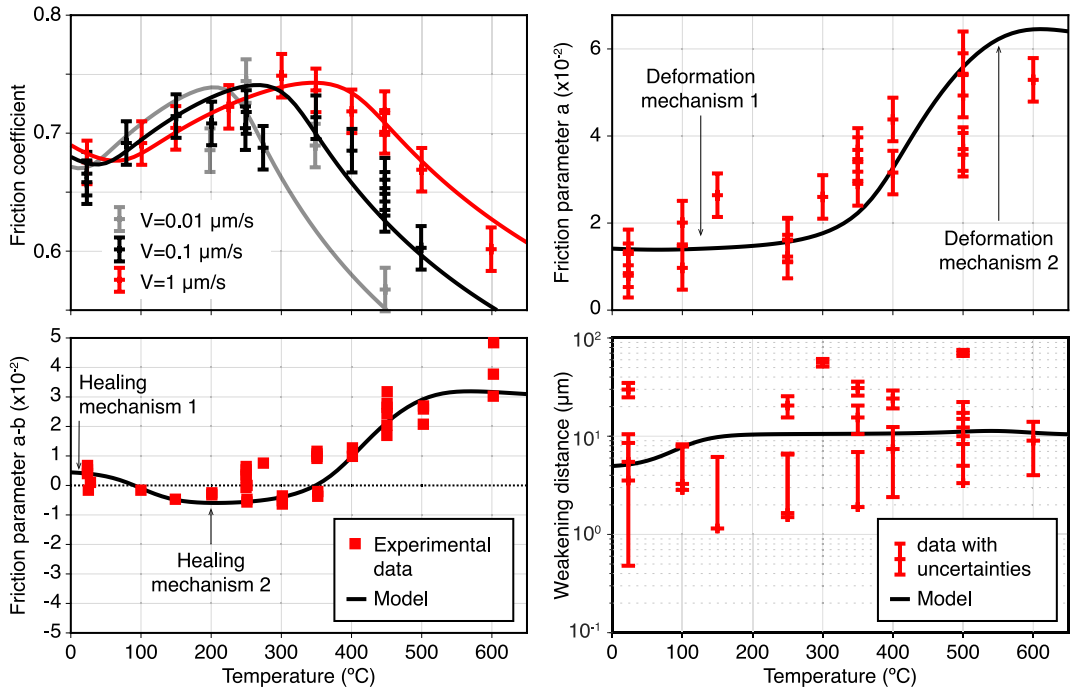

Figure 7. Evolution of the frictional properties of Westerly granite synthetic gouge in wet conditions with temperature and velocity (Blanpied et al., 1995, 1998) and comparison with the constitutive model described in Section 2. (a) Temperature and velocity dependence of the steady-state coefficient of friction at $V = 0.01$ µm/s (gray), $V = 0.1$ µm/s (black), and $V = 1$ µm/s (red) from room temperature (23°C) to 600°C. The modeled frictional response is shown with colored solid lines for the corresponding velocities. The temperature-weakening, velocity-strengthening regime above 350°C corresponds to the transition to the second deformation mechanism. (b) Temperature dependence of the direct effect parameter a with temperature (red errorbars) and constitutive model (solid line). (c) Temperature dependence of the steady-state velocity dependence parameter $a - b$ (red squares) and constitutive model (solid line). The low-temperature transition from steady-state velocity-strengthening to velocity-weakening is caused by a change of healing mechanism. The high-temperature transition from velocity-weakening to velocity-strengthening is caused by a change of deformation mechanism. (d) Evolution of the characteristic weakening distance (red errorbars) and prediction from the model (solid black line). The model predictions in panels (a–d) emanate from a single set of constitutive parameters listed in Table 2.

a satisfactory model for $\alpha = 0.06$, $n_1 = 50$, $n_2 = 12$, $Q_1 = 40$ kJ/mol, $Q_2 = 70$ kJ/mol, $\bar{T}_1 = 20$°C, $\bar{T}_2 = 290$°C, $p_1 = 4.5$, $p_2 = 2.1$, $H_1 = 35$ kJ/mol, $H_2 = 55$ kJ/mol, $T_1 = 0$°C, and $T_2 = 75$°C with $m_k = \alpha n_k$. The complete list of parameters is presented in Table 2. Despite the apparent complexity of the model, the constitutive parameters are individually constrained by specific observations. The power exponents n_k of the deformation mechanisms are tightly constrained by the low- and high-temperature values of a. The power exponents p_k of the healing mechanisms derive from the distribution of $a - b$. Finally, the thermodynamic parameters affect the transition temperatures and the degree of temperature-weakening in the velocity-strengthening domains. The constitutive model explains the main features of the mechanical data, capturing the temperature dependence of direct effect and steady-state parameters and the friction coefficient, but also the velocity dependence of the friction coefficient within two orders of magnitude of slip-rate (Figure 7).

Given the capability of the model to explain complex laboratory data, we explore experiments that document frictional behavior for a wider range of velocities. We consider the frictional properties of core samples retrieved from the Deep Fault Drilling Project on the Alpine Fault, New Zealand (Niemeijer et al., 2016). The samples include cataclasites (AF1, AF2, AF4) and ultramylonites (AF5 and AF6). The gouge sample AF4 is derived from an active principal slip zone of the Alpine Fault. The composition of the natural samples consists of up to 80 wt% framework silicates with up to 10 wt% calcite and the remaining part filled with phyllosilicate minerals. Sample AF4 contains about 15 wt% smectite. The steady-state parameter $a - b$ is obtained in a series of velocity-step experiments conducted under effective normal stress of 90 MPa with a fluid pressure of 60 MPa. For samples AF1, AF2, AF5, and AF6, the velocity steps cover three orders of magnitude of slip-rate, from 0.3 to 300 µm/s, which is still below the transition to lubrication at slip-rates well above 1 mm/s. For sample AF4, the velocity

Table 2
Constitutive Parameters Used to Describe the Mechanical Data of Dry Albite (Nakatani, 2001), Wet Westerly Granite (Blanpied et al., 1995, 1998), Alpine Fault Samples AF1, AF2, AF4, AF5, and AF6 (Niemeijer et al., 2016), and Basalt (Okuda et al., 2023) Gouge

Physical parameter	Symbol	Albite	Granite	AF1	AF2	AF4	AF5	AF6	Basalt
Reference friction	μ_0	0.74	0.66	0.70	0.70	0.70	0.70	0.70	0.57
Asperity size exponent	α	0.04	0.06	0.10	0.10	0.10	0.10	0.1	0.05
Stress power exponent	n_1	75	50	30	30	30	30	30	30
	n_2	23	12	10	10	12	10	10	30
Activation energy	Q_1 (kJ/mol)	50	40	30	30	30	30	30	40
	Q_2 (kJ/mol)	65	70	85	85	120	55	120	80
Activation temperature	$\bar{T}_1$ (°C)	20	20	20	30	20	20	20	20
	$\bar{T}_2$ (°C)	290	290	315	330	330	245	390	400
Healing power exponent	p_1	–	4.5	4.5	4.5	4.5	4.5	4.5	3.15
	p_2	–	2.1	1.65	1.65	1.5	2.1	1.8	1.2
Healing activation energy	H_1 (kJ/mol)	–	35	30	30	30	30	30	35
	H_2 (kJ/mol)	–	55	55	45	40	35	30	40
Healing reference temperature	T_1 (°C)	–	0	0	20	0	0	0	0
	T_2 (°C)	–	75	120	100	125	55	60	75

Note. In all cases, we use $V_0 = 1$ μm/s and $d_0 = 1$ μm. We systematically use $G_k = (1\,\mu\text{m})^{p_k}$/s and $m_k = \alpha n_k$ for $k = 1, 2$, except for basalt, for which we use $m_2 = 0$.

steps cover five orders of magnitude, from 3 nm/s to 300 μm/s. The experiments focus on the steady-state behavior, constraining the steady-state velocity dependence parameter $a - b$. In the velocity-weakening regime, the spontaneous occurrence of stick-slip events complicates the determination of $a - b$ experimentally.

Among the Alpine Fault natural gouge samples, we first consider AF1 from the upper foliated cataclasite that contains more than 30 wt% quartz, 10–30 wt% albite, and less than 10 wt% chlorite and calcite. The mechanical data reveal three steady-state frictional regimes with velocity-strengthening below 100°C, velocity-weakening between 200 and 400°C, and a second velocity-strengthening regime at high temperatures and slip-rates below 20 μm/s (Figure 8a). The distribution of the velocity-strengthening and velocity-weakening domains is compatible with the competition between two thermally activated healing mechanisms at temperatures lower than 300°C and the competition between two deformation mechanisms at temperatures above 400°C. To explain the data quantitatively, we optimize the constitutive parameters by grid search. The two deformation mechanisms are characterized by $\alpha = 0.1$, $n_1 = 30$, $n_2 = 10$, $Q_1 = 30$ kJ/mol, $Q_2 = 85$ kJ/mol, $\bar{T}_1 = 20$°C, $\bar{T}_2 = 315$°C with $m_k = \alpha n_k$. The two healing mechanisms are defined by $p_1 = 4.5$, $p_2 = 1.65$, $H_1 = 30$ kJ/mol, $H_2 = 55$ kJ/mol, $T_1 = 0$°C, and $T_2 = 120$°C. The complete list of parameters is shown in Table 2. The model prediction is shown in Figures 8a and 8b. The model consistently explains all observations within uncertainty, except the large negative value of $a - b = -0.0395$ at 300°C and $V = 1$ μm/s (Figure 8b). At first order, the predicted pattern is a velocity-weakening region spanning 300° with a lower and higher temperature limit that depends on the sliding velocity. While the velocity-weakening region starts at 100°C at 1 μm/s, it requires a minimum temperature of 200°C at 300 μm/s.

Next, we consider sample AF2, from an unfoliated cataclasite unit that contains more than 30 wt% quartz, between 10 and 30 wt% microcline and sanidine, and minor amounts of phengite, chlorite, and calcite, each representing less than 10 wt%. The distribution of $a - b$ is similar to sample AF1, except for the temperature of the low-temperature transition from velocity-strengthening to velocity-weakening (Figure 8c). At a slip-rate of 1 μm/s, the velocity-weakening region spans from about 50 to 450°C. However, at slip-rates above 30 μm/s, all measurements indicate steady-state velocity-weakening above 200°C. Given the similar general distribution of $a - b$, the mechanical data can also be explained by the activation of two healing mechanisms and two deformation mechanisms. The low-temperature transition can be explained with the following parameters for the healing mechanisms: $p_1 = 4.5$, $p_2 = 1.65$, $H_1 = 30$ kJ/mol, $H_2 = 45$ kJ/mol, $T_1 = 0$°C, and $T_2 = 100$°C. The deformation mechanisms are almost identical to those of AF2, with $\alpha = 0.1$, $n_1 = 30$, $n_2 = 10$, $Q_1 = 30$ kJ/mol, $Q_2 = 85$ kJ/mol, $\bar{T}_1 = 20$°C, and $\bar{T}_2 = 330$°C. The model explains all the observations within uncertainties (Figure 8d).

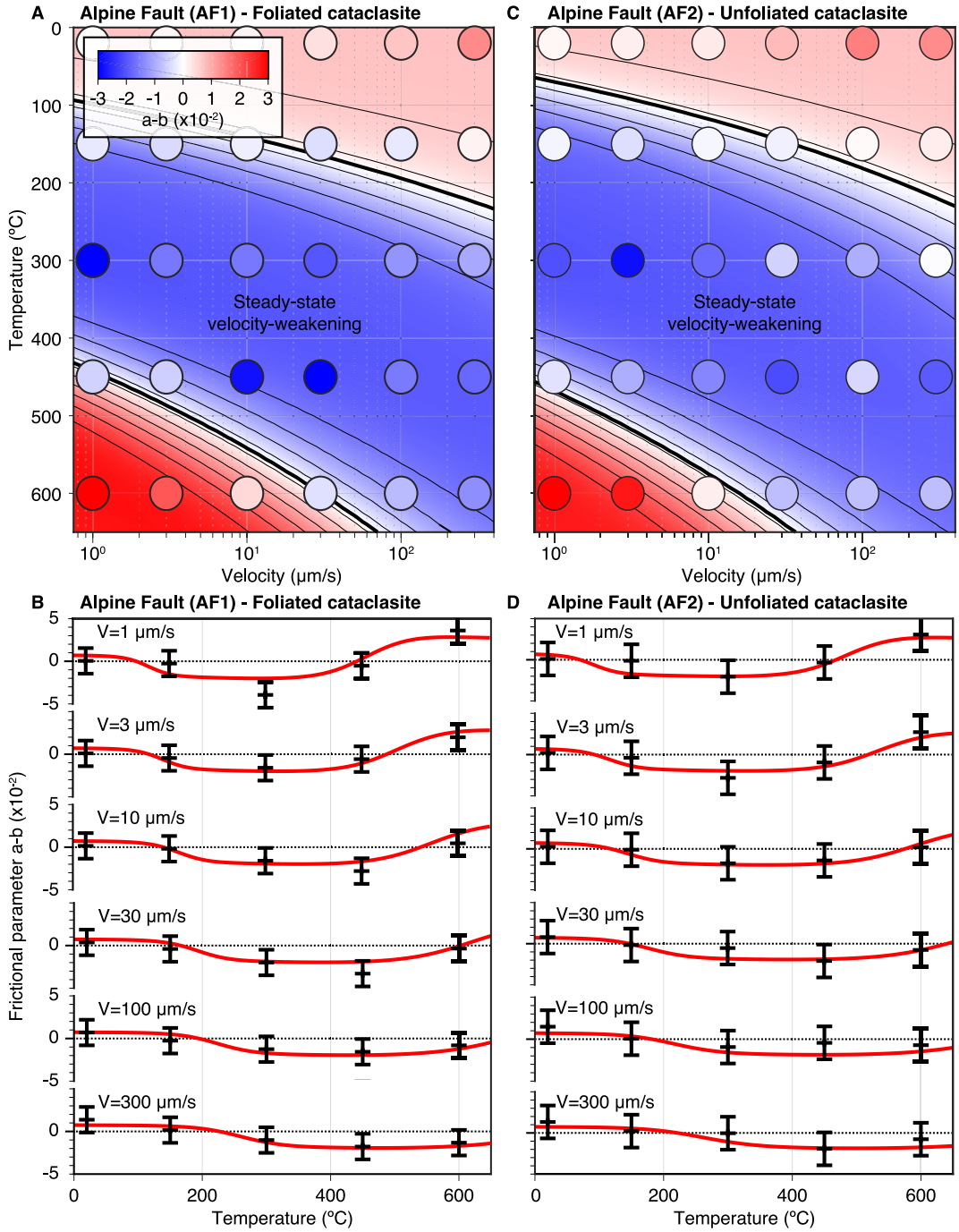

Figure 8. Observed and modeled frictional properties of natural samples of the Alpine Fault, New Zealand from the Gaunt Creek Deep Fault Drilling Project. (a) Evolution of the steady-state parameter $a - b$ with temperature and slip-rate (colored circles) and prediction of the constitutive model (background color) for the foliated cataclasite gouge of sample AF1. (b) Steady-state parameter $a - b$ from laboratory observations (error bars) and continuous predictions of the constitutive model (red profile). Panel (c) is the same as (a) for the unfoliated cataclasite gouge of sample AF2. Panel (d) is the same as (b) for sample AF2. The constitutive parameters are listed in Table 2.

We now examine the mechanical data for sample AF5, which contains a mixture of ultramylonitic and cataclastic gouge with >30 wt% albite, >30 wt% quartz, 10–30 wt% chlorite, and <10 wt% phlogopite and calcite. The distribution of the steady-state velocity-dependence parameter is shown in Figure 9a. At a slip-rate of 1 μm/s, the velocity-weakening regime operates at low-temperature, between 50 and 350°C. The first, low-temperature

transition can be explained by the competition between two healing mechanisms under the same prevailing deformation mechanism with $p_1 = 4.5$, $p_2 = 2.1$, $H_1 = 30$ kJ/mol, $H_2 = 35$ kJ/mol, $T_1 = 0$°C, and $T_2 = 55$°C. The second, high-temperature transition can be explained by the competition of two thermally activated deformation mechanisms with $\alpha = 0.1$, $n_1 = 30$, $n_2 = 10$, $Q_1 = 30$ kJ/mol, $Q_2 = 55$ kJ/mol, $\bar{T}_1 = 20$°C, and $\bar{T}_2 = 245$°C with $m_k = \alpha n_k$. The model explains virtually all the observations within uncertainties, except for the particularly strong velocity-weakening at 600°C and 300 μm/s (Figure 9b).

The AF6 gouge originates from an ultramylonite unit with more than 30 wt% oligoclase and quartz, between 10 and 30 wt% chlorite, and less than 10 wt% calcite and phlogopite. The distribution of $a - b$ with temperature and slip-rate is shown in Figure 9c, exhibiting a wide velocity-weakening regime from room temperature to 500°C at low slip-rate (1 μm/s). However, fast slip ($V > 100$ μm/s) is restricted below 250°C. The low-temperature transition can be explained with two healing mechanisms characterized by $p_1 = 4.5$, $p_2 = 1.8$, $H_1 = 30$ kJ/mol, $H_2 = 30$ kJ/mol, $T_1 = 0$°C, and $T_2 = 60$°C. The second transition at high temperatures can be explained by two deformation mechanisms with $\alpha = 0.1$, $n_1 = 30$, $n_2 = 10$, $Q_1 = 30$ kJ/mol, $Q_2 = 120$ kJ/mol, $\bar{T}_1 = 20$°C, and $\bar{T}_2 = 390$°C. The model can explain all the observations within uncertainties.

Given the success of the model on the Alpine Fault gouge samples, we now consider the low slip-rate experiments conducted on sample AF4, with the imposed velocities ranging from 3 nm/s to 300 μm/s, while consistently exploring the impact of temperatures from 23 to 600°C (Figure 2a). Sample AF4 is extracted from the upper principal slip zone of the Alpine Fault near Gaunt Creek in the Deep Fault Drilling Project 1B borehole. The sample contains quartz, labradorite oligoclase, and smectite, all in low proportions between 10 and 30 wt%. The mechanical data is still compatible with the thermal activation of competing healing and deformation mechanisms, except for an outlier at 10 nm/s and 600°C showing velocity-weakening. The low-temperature transition can be explained with two healing mechanisms characterized by $p_1 = 4.5$, $p_2 = 1.5$, $H_1 = 30$ kJ/mol, $H_2 = 40$ kJ/mol, $T_1 = 0$°C, and $T_2 = 125$°C. The high-temperature transition can be explained with two deformation mechanisms with $\alpha = 0.1$, $n_1 = 30$, $n_2 = 12$, $Q_1 = 30$ kJ/mol, $Q_2 = 120$ kJ/mol, $\bar{T}_1 = 20$°C, and $\bar{T}_2 = 330$°C (Figure 10). The model explains most measurements within uncertainties, but severely underpredicts two large velocity-weakening responses at 300°C and one large velocity-strengthening response at 300 μm/s. The constitutive framework provides otherwise a satisfactory model for five orders of magnitude of slip-rates from room temperature to 600°C.

Finally, we focus on the mechanical data for basalt gouge (Okuda et al., 2023). The gouge is collected from an altered basaltic rock that outcrops the exhumed Mugi Mélange in the Shimanto accretionary complex in southwest Japan. The sample is composed of 50% albitized plagioclase, 27% clinopyroxene, 15% chlorite. The steady-state friction coefficient and velocity dependence parameter are estimated in velocity-steps experiments from 1 to 100 μm/s from 100 to 550°C under effective normal stress of 100 MPa with pore-fluid pressure of 100 MPa. The velocity-step experiments are conducted at different temperatures in subsequent stages of the same experiment as strain accrues. The mechanical data are shown in Figure 11, revealing three distinct frictional regimes with a steady-state velocity-strengthening to velocity-strengthening transition at low temperature and a second transition to velocity-strengthening at high temperature that depends on slip-rate. The steady-state friction coefficient is relatively uniform around 0.6 with a possible softening to 0.45 at 550°C and 1 μm/s. As the measurements are conducted in different stages, the measurements are not entirely consistent, showing appreciable differences in measured properties at the same temperature and slip-rate. These issues are ubiquitous in laboratory experiments because the samples harden substantially as the texture matures with accumulated shear.

These shortcomings notwithstanding, we model the mechanical data invoking the competition between several healing and deformation mechanisms (Figure 11). The low-temperature transition to steady-state velocity-weakening can be explained by two healing mechanisms and the second transition to velocity-strengthening at higher temperature is compatible with the activation of a second deformation mechanism. Only the experiments at slip-rates of 10 and 100 μm/s show a continuous function of $a - b$ with temperature and the model explains these data within uncertainties (Figure 11b). For the other experiments at 3 and 30 μm/s, it is unclear at which temperature the transition to velocity-strengthening occurs. For the distribution of the friction coefficient at steady-state, all the experiments show substantial gaps across different ranges of temperature, complicating the interpretation. Given these issues, we cannot firmly conclude on the merit of the model regarding the evolution of the friction coefficient. We therefore focus the analysis on the detailed frictional response upon velocity steps (Figures 11e and 11f).

The velocity steps conducted at 150°C at velocities from 1 to 100 μm/s (run number u968, stage 2) exhibit a transition from steady-state velocity-weakening, to velocity-neutral, to velocity-strengthening with a similar

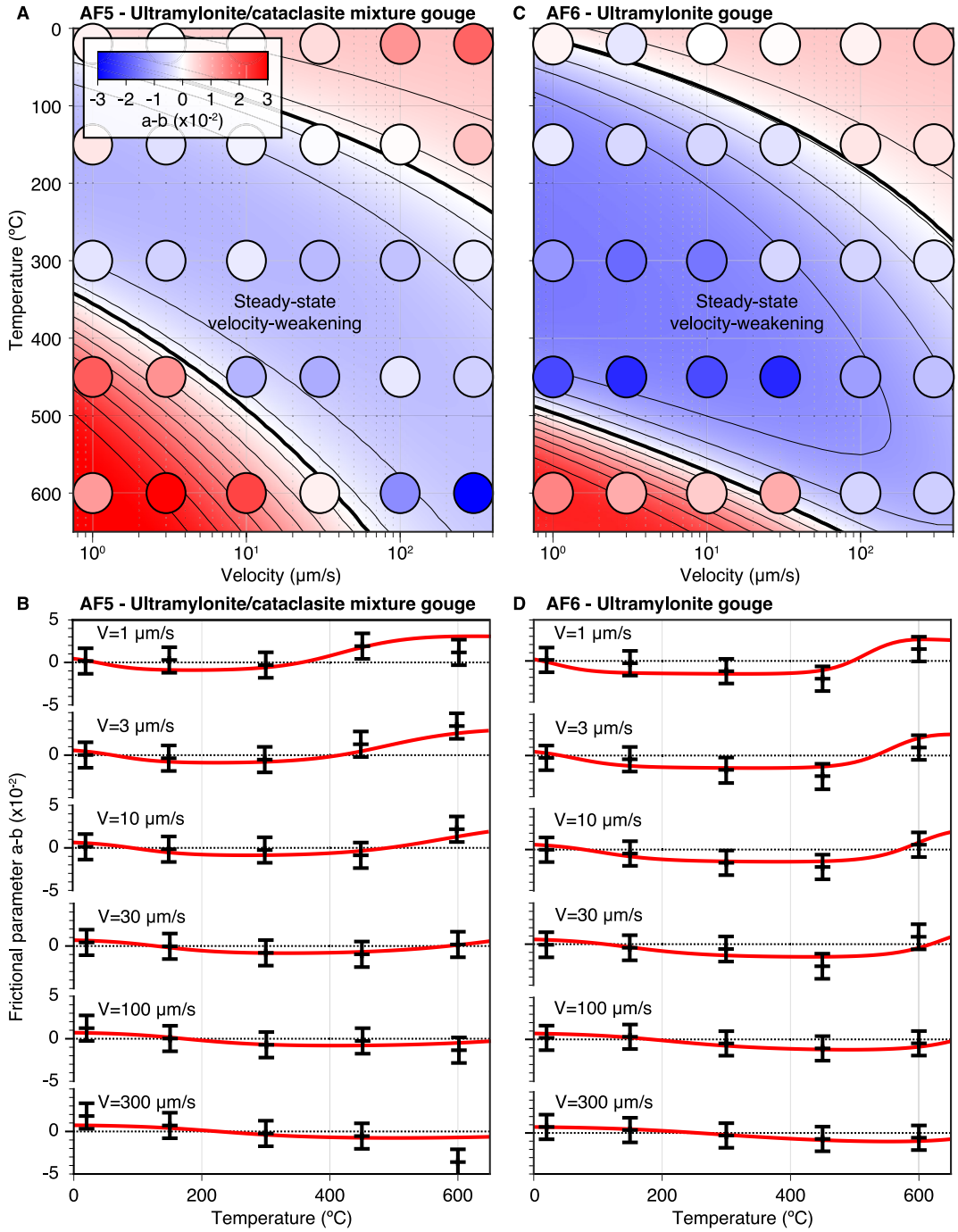

Figure 9. Observed and modeled frictional properties of natural samples of the Alpine Fault, New Zealand for ultramylonite gouge. (a) Evolution of the steady-state parameter $a - b$ with temperature and slip-rate (colored circles) and prediction of the constitutive model (background color) for the ultramylonite/cataclasite gouge of sample AF5. (b) Steady-state parameter $a - b$ from laboratory observations (error bars) and continuous predictions of the constitutive model (red profile). Panel (c) is the same as (a) for the ultramylonite gouge of sample AF6. Panel (d) is the same as (b) for sample AF6. The constitutive parameters are listed in Table 2.

direct effect, compatible with the transition of healing mechanism (Figure 11c). The measured and modeled response is smoothed by the finite stiffness $k = 0.3$ MPa/μm of the machine/sample assembly, which is optimized to fit the observations. The mechanical response at 500°C (run number u992, stage 3) is much different, with a rate-strengthening and work-hardening response at low velocity, transitioning to state-dependent

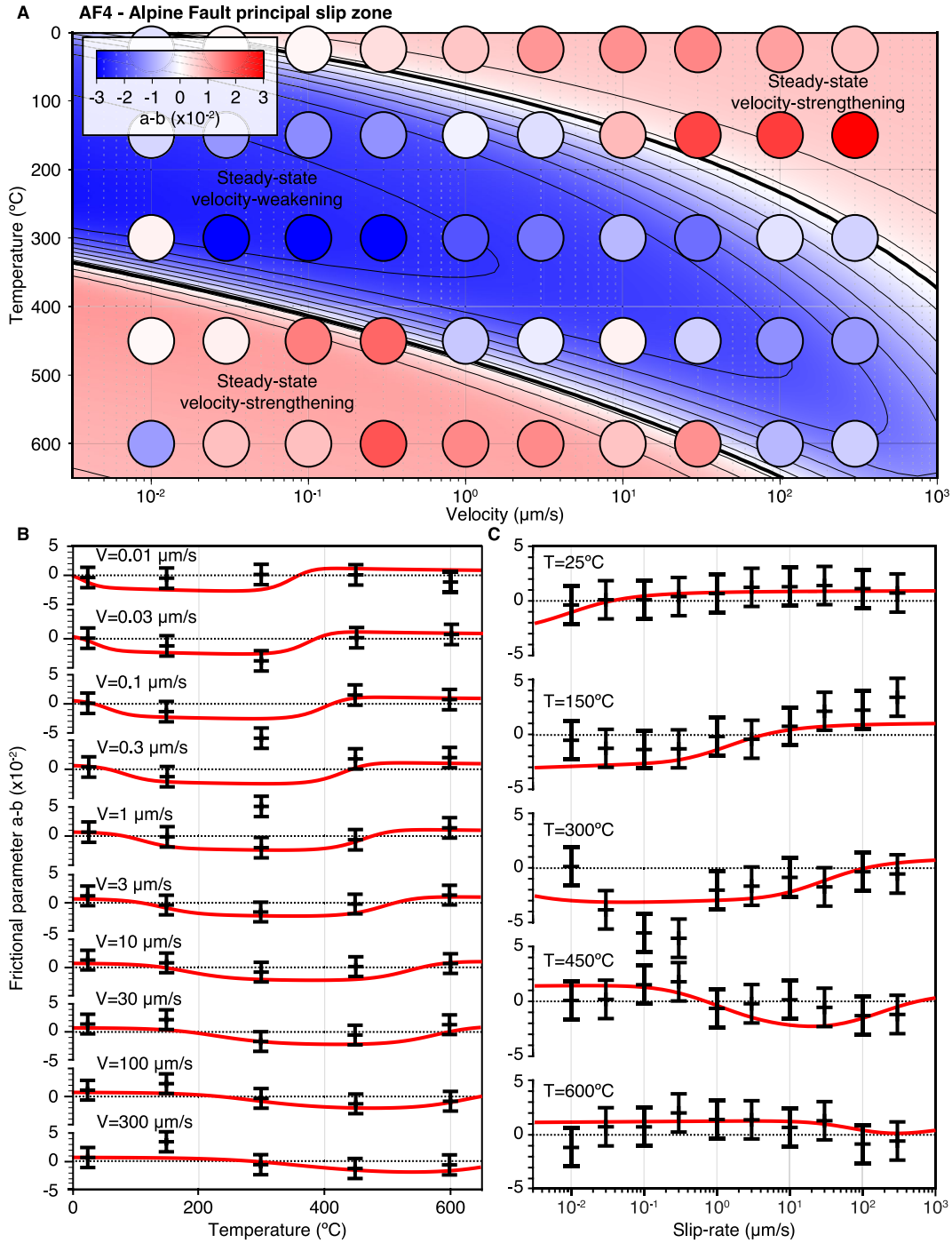

Figure 10. Observed and modeled frictional properties of natural samples of the principal slip zone of the Alpine Fault (gouge sample AF4). (a) Evolution of the steady-state parameter $a - b$ with temperature and slip-rate (colored circles) and prediction of the constitutive model (background color). (b) Steady-state parameter $a - b$ from laboratory observations (error bars) and continuous predictions of the constitutive model (red profile) as function of temperature for slip-rates from 0.01 to 300 µm/s. (c) Evolution of the steady-state parameter $a - b$ as a function of slip-rate for temperatures from 25 to 600°C. The velocity-weakening region lies in higher temperature ranges with increasing slip-rate. The constitutive parameters are listed in Table 2.

velocity-strengthening at the 10–30 µm/s step, to finally velocity-neutral at the 30–100 µm/s step (Figure 11d). The behavior at low and high temperature and different velocities can be explained by the proposed constitutive model with constant parameters assuming $P = 1$ brittle process and $M - P = 1$ ductile process characterized by

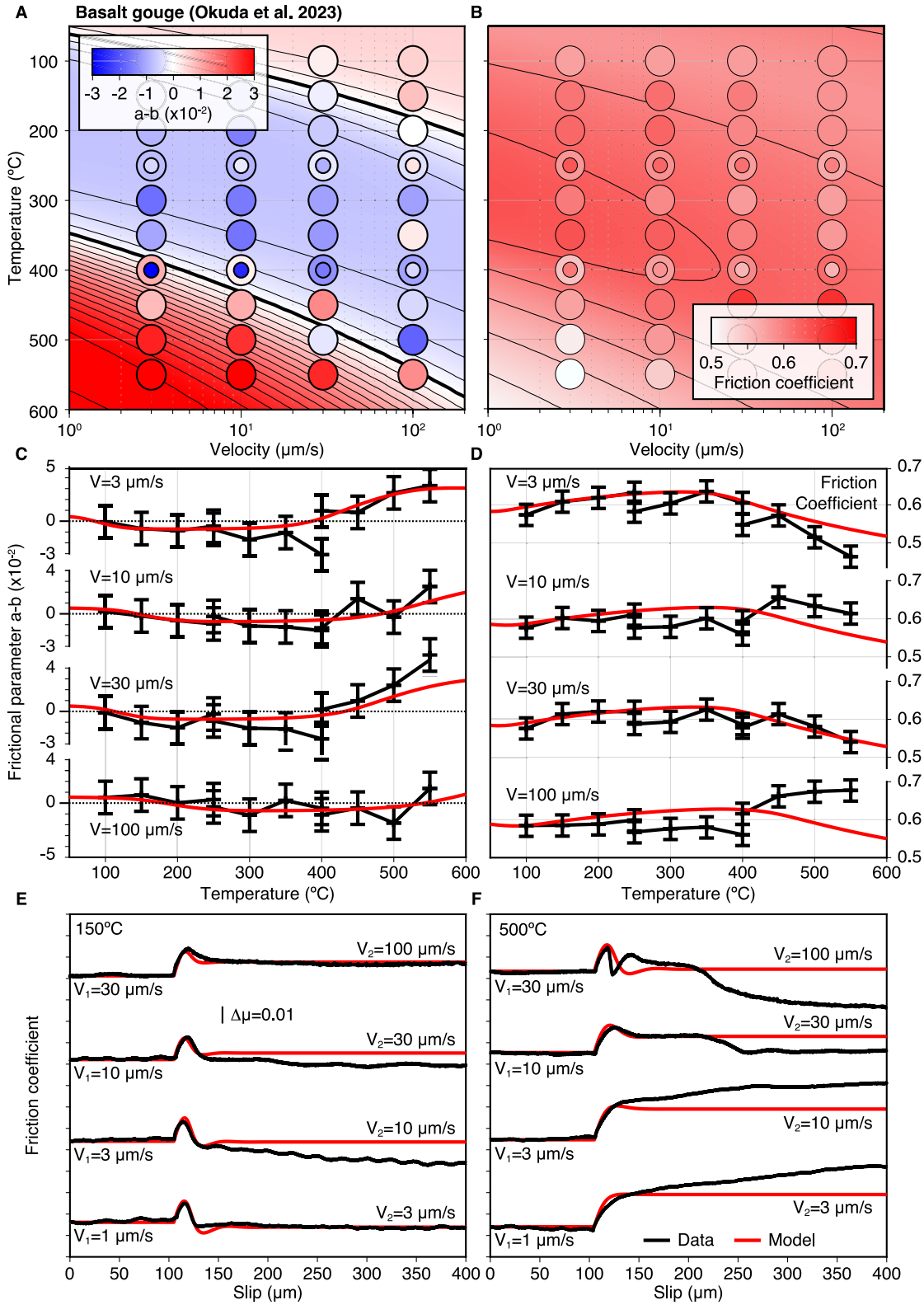

Figure 11.

$m_2 = 0$. To reproduce the direct and evolutionary effects, we use the slip-law end-member of Equation 8. The low-temperature transition requires $p_1 = 3.15$, $p_2 = 1.2$, $H_1 = 35$ kJ/mol, $H_2 = 40$ kJ/mol, $T_1 = 0$°C, and $T_2 = 75$°C. The transition to rate-dependent creep at high temperature can be obtained with $n_1 = n_2 = 30$, $m_1 = 1.5$, $m_2 = 0$, $Q_1 = 40$ kJ/mol, $Q_2 = 80$ kJ/mol, $\bar{T}_1 = 20$°C, and $\bar{T}_2 = 400$°C. The dominance of the direct effect for the second mechanism is captured by $m_2 = 0$, which suppresses the state dependence.

These results provide new constraints on the thermodynamics of fault friction. The deformation mechanisms exhibit activation energies in the range $Q = 30$–120 kJ/mol, with $Q = 30$–50 kJ/mol for cataclastic flow and $Q = 65$–120 kJ/mol for crystal plasticity (Table 2). This is compatible with activation energies of 10, 15, 25, and 50 kJ/mol for shale, granite, hornblende, and pyroxene and of 15 and 20–40 kJ/mol for natural gouges from the Longitudinal Valley Fault and the Alpine Fault in the frictional regime (Barbot, 2022). However, these values differ from $Q = 68$–101 kJ/mol for wet quartz gouge at temperatures between 24 and 82°C and effective pressure of 20 MPa (Chester, 1994). For the healing mechanisms, we find activation energies in the range $H = 30$–55 kJ/mol, but the range is narrower depending on the type of healing mechanism. For the healing mechanism that leads to steady-state velocity-strengthening, we find $H = 30$–35 kJ/mol. For the steady-state velocity-weakening regime, we find $H = 30$–55 kJ/mol. These results are similar to the ones for hornblende, pyroxene, and natural gouges in wet conditions, with $H = 20$–35 and $H = 30$–65 kJ/mol in the velocity-strengthening and velocity-weakening regimes, respectively (Barbot, 2022). The higher activation energy in the velocity-weakening regime is compatible with the low-temperature stability transition from steady-state velocity-strengthening to velocity-weakening at higher temperatures and seems a hallmark of gouge friction.

5. Discussion

The constitutive framework provides a rationale to understand the complex frictional behavior of fault gouge in the hydrothermal conditions relevant to the seismic cycle in the brittle lithosphere. The physics of fault friction is determined by rate-limiting processes at the micro-scale (Figure 12). Cataclastic flow mobilizes several deformation mechanisms, such as granular flow, comminution, and fracturing. As cracks propagate, Riedel shear zones form across the gouge. Slip on oblique Riedel shear zones (e.g., P, P', R, and R') and granular flow favor fault dilatancy under sliding. Strain can concentrate away from these fractures by extreme comminution, resulting in a heterogeneous deformation field with high strain localization. At high temperatures and low strain-rates, crystal plasticity within localized shear bands accommodates much of the deformation. In quartz, the transition to plasticity accompanies an increased concentration of intra-crystalline dislocation (Stesky, 1978b). As these processes are thermally activated and rate-dependent, the effective frictional properties become nonlinear functions of temperature and slip-rate.

Seismic cycles are enabled by healing between frictional instabilities (Figure 12b). Healing can be accompanied by compaction creep accommodated by viscoelastic collapse of micro-asperities or subcritical crack-growth at the tip of oblique fractures in dry and wet conditions. With atmospheric humidity or saturated fluids, pressure-solution creep may also consolidate the gouge by dissolution of highly stressed contacts and precipitation of ions in low-stress areas. Healing may also occur without compaction by cementation of the pore space and sealing of pre-existing cracks leading to the partial lithification of the pulverized gouge. In this case, deformation may localize in different regions of the gouge layer. The presence of water also modulates the rate of the deformation and healing processes. Atmospheric humidity or water-saturated pores induce stress corrosion at crack tips that modulate subcritical crack growth (Dunning et al., 1994). The presence of water also reduces the energy of activation of asperity creep by increasing the concentration of intra-crystalline defects (Karato & Jung, 2003; Rosa et al., 2005). Incorporating multiple thermally-activated healing mechanisms in the fault gouge explains many laboratory observations, including the transition from steady-state velocity-strengthening at room temperature to velocity-weakening at high temperatures (Figure 13a), but also the room-temperature transition from steady-state velocity-weakening to velocity-strengthening with increasing slip-rate that is commonly observed in

Figure 11. Frictional properties of basalt gouge under varied temperatures and slip-rates (Okuda et al., 2023). (a) Evolution of the steady-state parameter $a - b$ as a function of slip-rate and temperature from laboratory observations (colored circles) and prediction from the constitutive model (background color). Panel (b) is the same as (a) for the evolution of the steady-state friction coefficient. (c) Laboratory observations (black error bars) and constitutive model predictions (red solid line) for the evolution of $a - b$ with temperature and slip-rates. Experiments conducted in the same stage, defined by sample and cumulative slip, are connected by a solid black line. Panel (d) is the same as (c) for the coefficient of friction. (e) Frictional response to a velocity step for laboratory observations (black line) and constitutive model prediction (red line) at 150°C. The direct effect is smoothed by the machine/sample stiffness. Panel (f) is the same as (e) for an ambient temperature of 500°C.

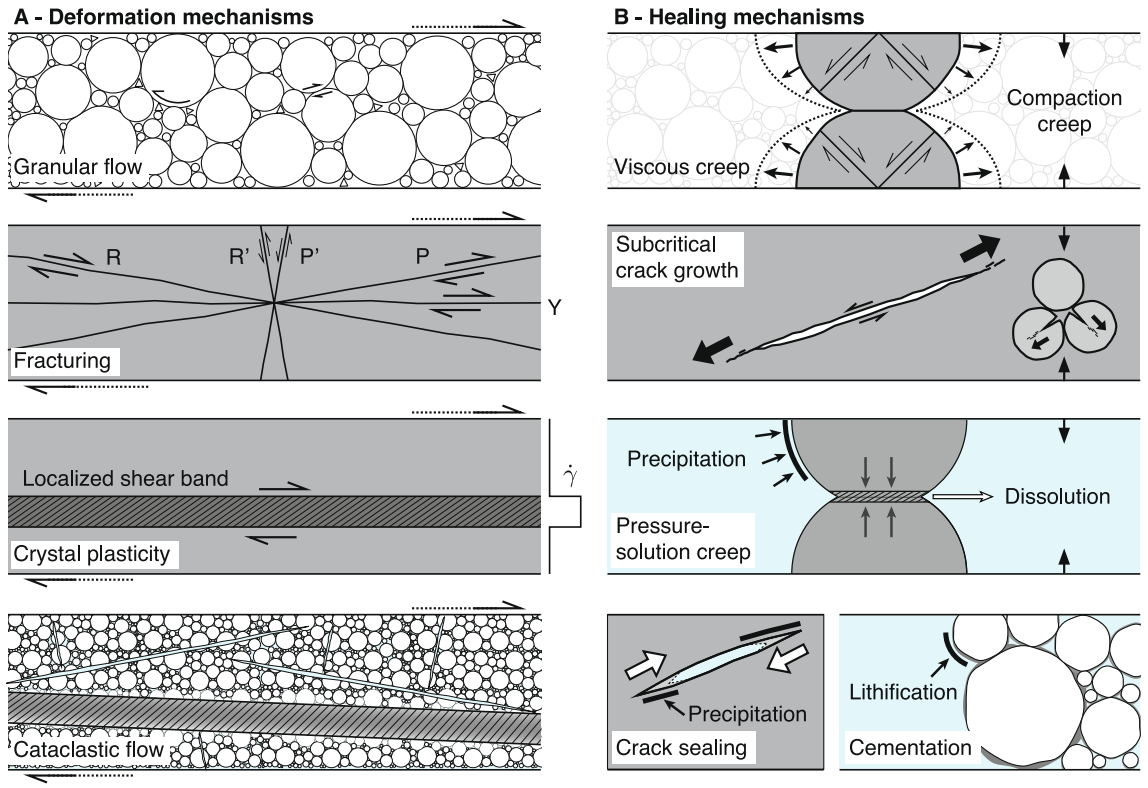

Figure 12. Schematic of competing deformation and healing mechanisms in fault gouge. (a) Deformation mechanisms leading to fault-parallel slip during cataclastic flow. Granular flow takes place by grain rolling, sliding, and neighbor swapping with vanishing activation energy. Fracturing involves slip along Riedel shear zones aligned with (Y) or oblique to (R, R', P, P') the fault zone. Crystal plasticity occurs by intra- and inter-granular flow within narrow shear bands in comminuted regions. Cataclastic flow incorporates the above mechanisms with contributions to fault slip in various amounts. (b) Time-dependent healing mechanisms. Viscoelastic creep increases the area of contact and flattens contact junctions. Subcritical crack growth accommodates gouge compaction by propagation of crack tips along Riedel fractures and across individual grains. Pressure-solution creep deforms micro-asperities by dissolution of the solid phase at contact junctions and precipitation in regions of low stress. Healing by cementation of pore space or crack sealing may not involve compaction.

the laboratory (e.g., Bureau et al., 2002; Reches & Lockner, 2010; Weeks, 1993, and references therein). Considering multiple deformation mechanisms, particularly the transition to crystal plasticity at higher temperatures and low strain-rates (J. Chen et al., 2020; Noda & Shimamoto, 2009, 2010; Shimamoto, 1986; L. Zhang & He, 2016), explains gouge friction for a wider range of lithologies and experimental conditions (Figure 13b).

With the proposed constitutive framework, we can now model friction and the transition to ductile behavior using a unified formulation with constant parameters in agreement with laboratory measurements. This implies that the mechanical response can be described based on lithology while still capturing the rate, state, and temperature dependence of rocks. Mechanical and structural models of the brittle lithosphere pairing a rock type with a set of constitutive properties under realistic loading conditions may explain important aspects of fault dynamics, including seismogenic potential and rupture style. The implications for our understanding of seismo-genesis in various tectonic settings are broad and substantial, with relevance to slow-slip events, tremors, and the rupture style of earthquakes.

The temperature dependence of gouge friction elucidates the relation between the seismogenic zone and geotherms in the continental lithosphere, which is dominated by a quartz-rich lithology. Based on results for wet quartz (Figure 7), the brittle layer can be divided into three frictional regimes: velocity-strengthening in the shallow crust, velocity-weakening in the seismogenic zone, and velocity-strengthening at higher temperatures. The seismogenic zone is confined within the temperature range of steady-state velocity-weakening at low slip rates, as earthquake nucleation operates at low slip speeds. The inhibition of coseismic slip at shallow depths explains the shallow slip deficit that is widely observed in continental settings (Barbot et al., 2023; Fialko et al., 2005; Hussain et al., 2016; Qiu et al., 2020). Other mechanisms may amplify this effect, such as plastic deformation of a damage zone surrounding the fault and propagation of fault slip on secondary fault branches in a flower structure. At subduction zones, the seismogenic zone is additionally controlled by lithological gradients, being bounded by

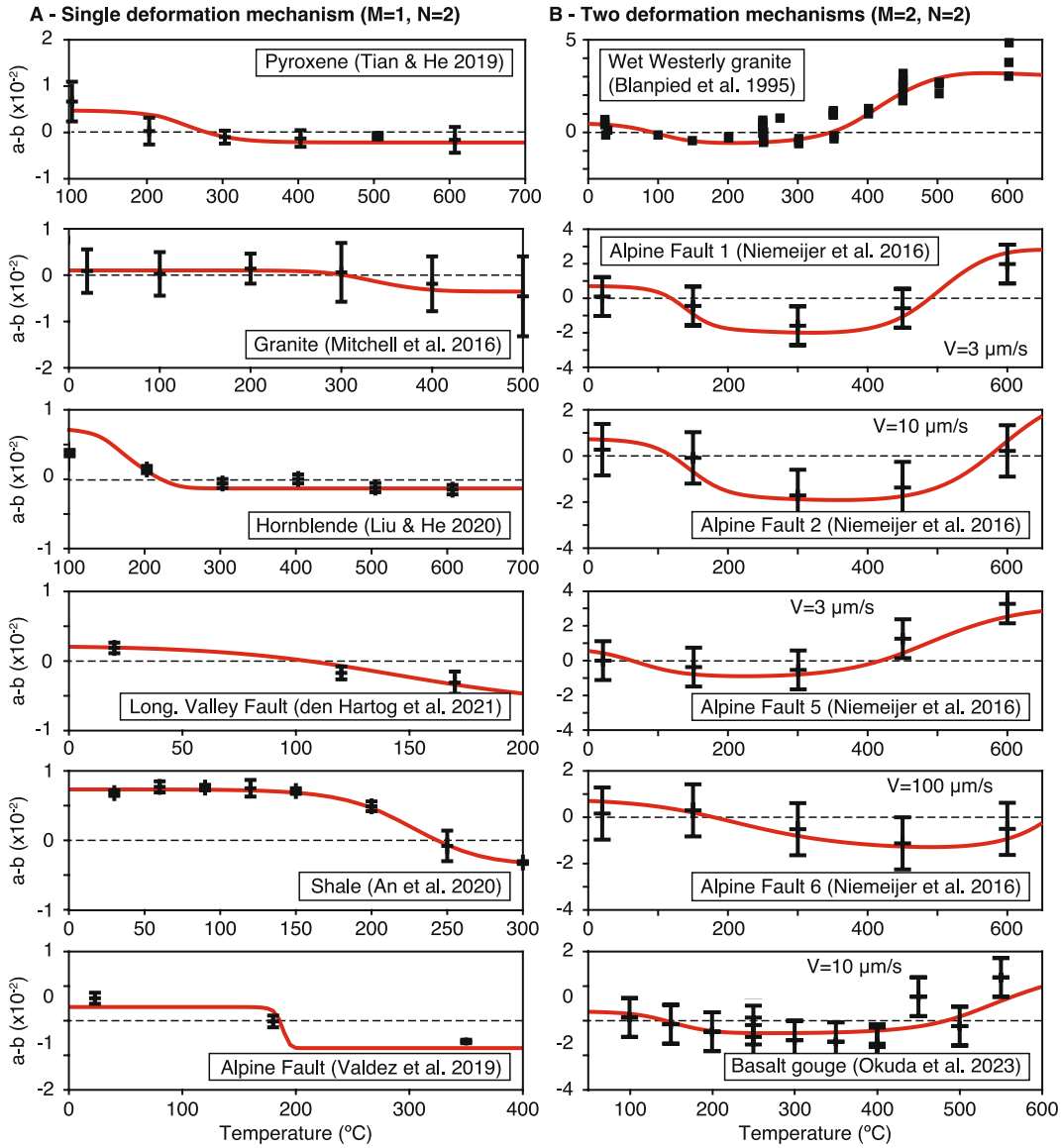

Figure 13. Thermal activation of gouge friction. (a) The frictional response of pyroxene (Tian & He, 2019), dry granite (Mitchell et al., 2016), and hornblende (Liu & He, 2020) synthetic gouges as well as shale (An et al., 2020) and other (den Hartog et al., 2021; Valdez et al., 2019) natural gouges can be explained by a single deformation mechanism with the competition between two thermally-activated healing mechanisms (Barbot, 2022). (b) Westerly granite (Blanpied et al., 1995, 1998), basalt (Okuda et al., 2023), and Alpine Fault gouges (Niemeijer et al., 2016) require a second deformation mechanism to explain restrengthening at high temperatures.

clay-rich sediments in the accretionary prism and a serpentinite metamorphic belt in the cold nose (Goswami & Barbot, 2018; Qiu & Barbot, 2022). At oceanic transforms, the temperature and slip-rate dependence of gabbro and peridotite friction may also explain the shallow confinement of the seismogenic zone, but the serpentinization of mantle rocks may affect the rupture style, producing earthquake swarms, slow-slip events, and tremors (A. Kohli et al., 2021; Kuna et al., 2019). Due to shear heating, the fault behavior at any depth may be complex, traversing the different frictional regimes dynamically as a function of evolving temperature and slip-rate during rupture nucleation and propagation. For example, the propagation of coseismic rupture throughout the entire brittle lithosphere along a fracture zone during the 2012 Mw 8.6 Indian Ocean earthquake (Wei et al., 2013) may have been facilitated by the velocity-weakening regime at high temperature for sufficiently high slip speed. Seismic swarms can be explained by temperature-hardening during shear heating that leads to apparent work-hardening (B. Wang & Barbot, 2023).

The constitutive framework offers several mechanisms for the generation of slow-slip events and tremors that are found in various tectonic settings. First, silent (aseismic) slow-slip events may develop in a stable-weakening regime whereby nucleation is aborted by a lack of accommodation space (Barbot, 2020b; D. Li & Liu, 2017; Liu & Rice, 2005). Depending on detailed parameters near the stability transition, slow-slip may manifest itself by long-term waves of partial coupling that take decades to unfold (Nie & Barbot, 2021). These behaviors may occur in a simple constitutive regime without change of healing or deformation mechanisms. Another path to slow-slip ruptures involves the competition between thermally activated healing mechanisms leading to the v-shaped velocity-dependence of steady-state friction (e.g., Bar-Sinai et al., 2014; J. Chen, 2023; Im et al., 2020; Okubo, 1989; Shibazaki & Shimamoto, 2007). At low-temperature, the frictional response of many gouges allows nucleation, but the transition to steady-state velocity-strengthening at higher slip-rates prevents rupture propagation. The failed nucleation results in an aseismic slow-slip event. These modes of slow-slip generation are appealing for their simplicity, but they cannot explain the synchronicity between slow slip and tremors that is widely observed at subduction zones (Ito et al., 2007; Obara & Kato, 2016; Rogers & Dragert, 2003; Schwartz & Rokosky, 2007). Simultaneous tremor and slow-slip events can be explained with homogeneous constitutive parameters in a velocity-weakening, temperature-hardening regime. Steady-state velocity-weakening allows nucleation, but the rapid strengthening by shear heating at high slip speed prevents the propagation of rupture at seismic speeds, resulting in the emergence of slow earthquakes following the slow-slip rupture front (B. Wang & Barbot, 2023). A final type of slow-slip event occurs in a velocity-strengthening, temperature-softening regime by spontaneous thermal instabilities due to the positive feedback with shear heating, explaining the rare occurrence of slow slip at mid-crustal depths in a continental setting (L. Wang & Barbot, 2020).

Despite some differences in the detailed implementation, the proposed constitutive framework shares fundamental assumptions with other theoretical models of fault friction. The physical processes accommodating deformation and healing are thermally activated (Brechet & Estrin, 1994; Chester, 1994, 1995; Heslot et al., 1994; Molinari & Perfettini, 2019; Nakatani, 2001; Nakatani & Scholz, 2004; Rice et al., 2001; Sleep, 1997) and gouge friction may involve several deformation mechanisms (Blanpied et al., 1995, 1998; J. Chen, 2023; J. Chen et al., 2021; Chester, 1994). But most importantly, the state variables that encapsulate the evolutionary effects originate from measurable physical quantities, may it be the real area of contact (Aharonov & Scholz, 2018, 2019; Bar-Sinai et al., 2014; Barbot, 2019b, 2022; Boitnott et al., 1992; Bowden & Tabor, 1964; Sleep, 2006) or the porosity (J. Chen, 2023; J. Chen & Spiers, 2016; J. Chen et al., 2017; Sleep, 2005). The evolving texture of the fault gouge influences other observables, including fluid permeability (Im et al., 2019; Proctor et al., 2020), electrical conductivity (Yamashita et al., 2014), acoustic transmissivity (Fukuyama et al., 2019; Kocharyan et al., 2018; Nagata et al., 2008, 2012; Rouet-Leduc et al., 2018), optical transparency and reflectivity (Bayart et al., 2018; Ben-David et al., 2010; Dieterich & Kilgore, 1994; Rubinstein et al., 2004; Selvadurai & Glaser, 2015, 2017), fault compaction and dilatancy (Carpenter, Ikari, & Marone, 2016; Marone et al., 1990), and the density of off-fault damage (Goebel et al., 2014). Hence, these physical quantities can serve as proxies for state variables in nature or in the laboratory, potentially explaining subtle changes in crustal properties shortly before and after earthquakes (Brenguier et al., 2008; Kato & Ben-Zion, 2021; Y. Li et al., 1998). Although practical considerations need to be considered and further research is necessary, the relationships among state variables and their proxies may offer a physical basis for short-term earthquake prediction by active-source monitoring of faults. Textural changes within the fault zone during nucleation may be detectable before any strain occurs and well in advance of the radiation of seismic waves.

The proposed constitutive law offers a description of the behavior of gouge friction at low and intermediate slip-rates from room temperature to 600°C, capturing the different frictional regimes as a function of slip speed and temperature. The model is applicable to the nucleation and propagation of frictional instabilities that do not emanate substantial heat, but is inadequate to capture enhanced weakening at near-liquidus temperatures (Rice, 2006). Although strong weakening may occur by thermal softening of plastic shear bands with substantial shear heating, the model does not explicitly capture the formation of melt, silica gel, or another lubrication phase (Di Toro et al., 2004, 2006). The constitutive framework applies to a limited range of cumulative strain where the texture is preserved. How the constitutive parameters may evolve for large slip is currently undetermined. The model is readily compatible with thermal pressurization by thermal dilatancy of pore fluid (Noda & Lapusta, 2013) or fault zone pressurization by carbonate demineralization (Sulem & Famin, 2009), as both simply modulate the effective normal stress. Future work must incorporate the formation of pseudo-tachylites or other high-temperature products (Di Toro et al., 2005; Kirkpatrick et al., 2012; Pec et al., 2012; Rowe et al., 2018;

Rowe & Griffith, 2015) to capture the thermo-mechanical response of faults during seismic cycles for large earthquakes. Other considerations include the effect of gradual changes in pore fluid pressure that affect the frictional response beyond the Terzaghi effect (Bedford et al., 2021; Xing et al., 2019; L. Zhang & He, 2016) and the dependence of healing on normal stress (Linker & Dieterich, 1992; Sleep, 2005, 2006).

6. Conclusion

We describe a constitutive framework for gouge friction calibrated to extensive laboratory data that characterizes the frictional behavior of rocks for the hydrothermal conditions relevant to the brittle lithosphere. The model elucidates the mechanics of gouge deformation from room temperature to 600°C for slip-rates from nanometers to millimeters per second, which applies to creep, slow-slip events, afterslip, rupture nucleation, and the propagation of moderate-size earthquakes. The constitutive law relies on the thermal activation of competing healing mechanisms that increase the real area of contact at different rates depending on temperature and slip-rate. As a result, the frictional behavior is not stationary. In low-temperature, high-velocity conditions, the frictional response is dominated by cataclasis, implying extreme grain-size reduction and localization within the fault gouge. Crystal plasticity exhibits a different sensitivity to shear stress and temperature that stabilizes fault slip in high-temperature, low-velocity conditions. Accounting for these processes explains the mechanical data for many different types of synthetic and natural gouges with broad relevance to the seismic cycle in continental and oceanic tectonic settings.

The complex frictional response of fault gouge under such wide conditions can be captured by two mathematical equations, either Equations 4 and 7 or Equations 4 and 8, depending on the choice of evolution law. The physical model allows extrapolation of laboratory data to the conditions found throughout the brittle lithosphere, explaining fault rheology from the surface to the brittle-ductile transition. Although the details vary based on lithology, confining stress, and other factors, the model delineates three distinct regimes of stability that operate in different slip-rate and temperature conditions. The top of the seismogenic zone originates from a transition of healing mechanism within the brittle field. In contrast, the bottom of the seismogenic zone corresponds to the onset of semi-brittle deformation with a reduced sensitivity to the area of contact and a gradual transition to rate-dependent creep. The depths of key mechanical boundaries, such as the limits of the seismogenic zone and the brittle-ductile transition, are dynamic features that depend on fault slip-rate and temperature, which can vary greatly during the seismic cycle.

As the physical model concisely captures the rate, state, and temperature dependence of gouge friction, the constitutive behavior of faults may be described based on lithology and the ambient hydrothermal conditions, allowing more realistic predictions of fault dynamics and seismic hazards, including the seismogenic potential, recurrence patterns, and style of ruptures. Region-specific models of seismic activity may assimilate the thermo-mechanical properties of local rocks, requiring more systematic frictional experiments covering a wider range of temperature and slip-rate than is typically done. As the proposed physical model produces more complex and more realistic frictional behaviors than empirical friction laws, more research is needed to explore the implications for fault dynamics during the seismic cycle.

Appendix A: Relation Among Constitutive Parameters

In this appendix, we consider some analytic results that shed light on the frictional behavior and provide relationships among common constitutive parameters.

A1. Direct Effect Parameters

Without loss of generality, the rate-, state-, and temperature-dependence of friction can be characterized by the phenomenological parameters

$$n = \frac{\partial \ln V}{\partial \ln \tau}, \tag{A1}$$

$$m = \frac{\partial \ln V}{\partial \ln d}, \tag{A2}$$

and

$$Q = \frac{-\partial \ln V}{\partial (1/RT)} \quad . \tag{A3}$$

Within the assumptions of the model described in Section 2, the above parameters are constant regardless of velocity and temperature if a single deformation mechanism operates. However, when more deformation mechanisms are in force, these properties evolve gradually. To understand how, consider the velocity predicted by each mechanism

$$V_k = V_0 \left(\frac{\tau}{c_0 + \mu_0 \bar{\sigma}} \right)^{n_k} \left(\frac{d}{d_0} \right)^{\alpha n_k} \exp\left[-\frac{Q_k}{R} \left(\frac{1}{T} - \frac{1}{\tilde{T}_k} \right) \right], \tag{A4}$$

such that we can write the instantaneous velocity across the fault gouge as

$$V = \sum_{k=1}^{M} V_k(\tau, d, T). \tag{A5}$$

Applying the chain rule with Equations A1, A4, and A5 provides

$$\begin{aligned} n &= \frac{\partial \ln V}{\partial \ln \tau} = \frac{\tau}{V} \frac{\partial V}{\partial \tau} \\ &= \frac{\tau}{V} \sum_{k=1}^{M} \frac{\partial V_k}{\partial \tau} = \frac{\tau}{V} \sum_{k=1}^{M} \frac{n_k}{\tau} V_k \\ &= \sum_{k=1}^{M} n_k \frac{V_k}{V}, \end{aligned} \tag{A6}$$

showing that the power-law exponent varies as the weighted sum of the individual constitutive parameters n_k, where the weights V_k/V are the relative contributions of each mechanisms to the total velocity. A similar result can be found for the effective activation energy, using Equations A3–A5, with

$$\begin{aligned} Q &= \frac{-\partial \ln V}{\partial (1/RT)} = -\frac{1}{V} \frac{\partial V}{\partial (1/RT)} \\ &= -\frac{1}{V} \sum_{k=1}^{M} \frac{\partial V_k}{\partial (1/RT)} \\ &= \frac{1}{V} \sum_{k=1}^{M} Q_k V_k = \sum_{k=1}^{M} Q_k \frac{V_k}{V}. \end{aligned} \tag{A7}$$

For the direct effect of the state variable, a similar result holds, with

$$\begin{aligned} m &= \frac{\partial \ln V}{\partial \ln d} = \frac{d}{V} \frac{\partial V}{\partial d} \\ &= \frac{d}{V} \sum_{k=1}^{M} \frac{\partial V_k}{\partial d} = \frac{d}{V} \sum_{k=1}^{M} \frac{m_k}{d} V_k \\ &= \sum_{k=1}^{M} m_k \frac{V_k}{V}. \end{aligned} \tag{A8}$$

In addition, in the brittle regime where $m_k = \alpha n_k$, we always have $m = \alpha n$, regardless of the number of mechanisms.

A2. Steady-State Velocity Dependence

We now consider the steady-state frictional response, which determines fault stability. We start by investigating the velocity dependence. Without loss of generality, the rate-dependence of steady-state friction can be characterized by the phenomenological parameter

$$\frac{\partial \ln \tau_{ss}}{\partial \ln V}, \tag{A9}$$

where the subscript "ss" stands for "at steady-state." Applying the chain rule, the steady-state velocity dependence can be written

$$\frac{\partial \ln \tau_{ss}(V, d_{ss}(V))}{\partial \ln V} = \left.\frac{\partial \ln \tau_{ss}(V, d_{ss}(V))}{\partial \ln V}\right|_{d_{ss}} + \frac{\partial \ln \tau_{ss}(V, d_{ss}(V))}{\partial \ln d_{ss}} \frac{\partial \ln d_{ss}}{\partial \ln V}. \tag{A10}$$

Following Equation A1, we have

$$\left.\frac{\partial \ln \tau_{ss}(V, d_{ss}(V))}{\partial \ln V}\right|_{d_{ss}} = \frac{\partial \ln \tau}{\partial \ln V} = \frac{1}{n}. \tag{A11}$$

Combining Equations A1 and A2, we can write

$$\frac{m}{n} = \frac{\partial \ln \tau}{\partial \ln d}, \tag{A12}$$

which is general, but also applies in the steady-state condition of Equation A10. We can finally reduce Equation A10 by introducing the phenomenological parameter

$$p = -\frac{\partial \ln V}{\partial \ln d_{ss}}, \tag{A13}$$

which is defined in Equation 9 in the main text. With these definitions, we can write

$$\frac{\partial \ln \tau_{ss}(V, d_{ss}(V))}{\partial \ln V} = \frac{1}{n}\left(1 - \frac{m}{p}\right), \tag{A14}$$

which corresponds to Equation 10 in the main text. Hence, the frictional response is steady-state velocity-strengthening for $m < p$, velocity-neutral for $m = p$, and velocity-weakening for $m > p$. In the brittle regime, we have $m = \alpha n$, so we can write

$$\frac{\partial \ln \tau_{ss}}{\partial \ln V} = \frac{1}{n} - \frac{\alpha}{p}. \tag{A15}$$

In this case, the frictional response is steady-state velocity-strengthening for $\alpha n < p$, velocity-neutral for $\alpha n = p$, and velocity-weakening for $\alpha n > p$.

A3. Steady-State Temperature Dependence

We follow a similar procedure to describe the temperature dependence at steady-state, which can be characterized by

$$\frac{\partial \ln \tau_{ss}}{\partial 1/(RT)}. \tag{A16}$$

Applying the chain rule, the steady-state temperature dependence can be written

$$\frac{\partial \ln \tau_{ss}(T, d_{ss}(T))}{\partial (1/RT)} = \frac{\partial \ln \tau_{ss}(T, d_{ss})}{\partial (1/RT)} + \frac{\partial \ln \tau_{ss}(T, d_{ss})}{\partial \ln d_{ss}} \frac{\partial \ln d_{ss}}{\partial (1/RT)}. \tag{A17}$$

Using canonical relationships for partial derivatives and incorporating Equations A1 and A3, we have

$$\left(\frac{\partial \ln \tau_{ss}}{\partial (1/RT)}\right)_V = -\left(\frac{\ln V}{\partial (1/RT)}\right)_\tau \Big/ \left(\frac{\partial \ln V}{\partial \ln \tau}\right)_T = \frac{Q}{n}. \tag{A18}$$

Similarly, introducing the phenomenological parameter

$$H = -\left.\frac{\partial \ln V}{\partial (1/RT)}\right|_{d=0}, \tag{A19}$$

and using Equation A13, we have

$$\begin{aligned}\left(\frac{\partial \ln d_{ss}}{\partial (1/RT)}\right)_V &= -\left(\frac{\ln V}{\partial (1/RT)}\right)_\tau \Big/ \left(\frac{\partial \ln V}{\partial \ln d_{ss}}\right)_T \\ &= -\frac{H}{p}.\end{aligned} \tag{A20}$$

Finally, combining Equations A12, A18, and A20, Equation A17 simplifies to

$$\frac{\partial \ln \tau_{ss}(T, d_{ss}(T))}{\partial (1/RT)} = \frac{Q}{n} - \frac{mH}{np}, \tag{A21}$$

which corresponds to Equation 10 in the main text. The frictional response is steady-state temperature-hardening for $mH > pQ$, temperature-neutral for $mH = pQ$, and temperature-weakening for $mH < pQ$. In the brittle field, we have $m = \alpha n$, so this further simplifies to

$$\frac{\partial \ln \tau_{ss}}{\partial (1/RT)} = \frac{Q}{n} - \alpha \frac{H}{p}, \tag{A22}$$

In this case, the frictional response is steady-state temperature-hardening for $\alpha nH > pQ$, temperature-neutral for $\alpha nH = pQ$, and temperature-weakening for $\alpha nH < pQ$.

A4. Relations Among Frictional Parameters

In laboratory and theoretical studies, the direct and steady-state frictional responses are commonly described by the empirical parameters

$$\begin{aligned}a &= \frac{\partial \mu}{\partial \ln V} \\ a - b &= \frac{\partial \mu_{ss}}{\partial \ln V},\end{aligned} \tag{A23}$$

respectively, where the subscript "ss" refers to steady-state condition. The frictional parameter a is related to the constitutive parameters introduced in Section 2. Using Equation A1, we can write

$$\begin{aligned}a &= \frac{\partial \mu}{\partial \ln V} = \frac{\partial}{\partial \ln V}\frac{\partial \tau}{\partial \sigma} \\ &= \frac{\partial}{\partial \sigma}\frac{\partial \tau}{\partial \ln V} = \frac{\partial}{\partial \sigma}\left[\tau \frac{\partial \ln \tau}{\partial \ln V}\right] \\ &= \frac{\partial}{\partial \sigma}\left[\frac{\tau}{n}\right] = \frac{\mu}{n},\end{aligned} \tag{A24}$$

where we have used Equation A1 and $\partial\tau/\partial\sigma = \mu$. This explains Equation 12 in the main text. As the effective power-law exponent reduces with increasing temperatures or decreasing velocities, the effective parameter a increases. We can follow similar steps at steady-state using Equation A15, providing

$$\begin{aligned}a - b &= \frac{\partial \mu_{ss}}{\partial \ln V} = \frac{\partial^2 \tau_{ss}}{\partial \sigma\, \partial \ln V} \\ &= \frac{\partial}{\partial \sigma}\frac{\partial \tau_{ss}}{\partial \ln V} = \frac{\partial}{\partial \sigma}\left(\tau \frac{\partial \ln \tau_{ss}}{\partial \ln V}\right) \\ &= \frac{\mu}{n}\left(1 - \frac{m}{p}\right)\end{aligned} \tag{A25}$$

Hence, variations of m, n, and p have a strict equivalence to variations of a and $a - b$. A further simplification occurs in the brittle field using $m = \alpha n$.

Appendix B: Numerical Velocity Jumps Experiments

In Section 3, we conduct numerical velocity-step experiments to explore the variations of frictional properties with temperature and velocity. In Section 4, we use velocity-step experiments to reproduce laboratory observations. We provide the detailed procedure in this Appendix. Considering a slider at steady-state at velocity V_1, we impose an instantaneous jump to a velocity V_2 at constant state and simulate the evolutionary phase to the new steady-state. To calculate the steady solution at any temperature and velocity V_1, we solve for the steady-state micro-asperity size that satisfies Equation 7 or Equation 8 for $\dot{d} = 0$, providing

$$V_1 = \frac{2h}{\lambda} \sum_{k=1}^{N} \frac{G_k}{p_k d_{ss}^{p_k}} \exp\left[-\frac{H_k}{R}\left(\frac{1}{T} - \frac{1}{T_k}\right)\right]. \tag{B1}$$

There is no closed-form solution, so we find the root of this transcendental equation numerically. Equipped with the steady-state micro-asperity size d_{ss}, we solve for the shear stress that satisfies

$$V_1 = \sum_{k=1}^{M} V_0 \left(\frac{\tau_1}{c_0 + \mu_0 \bar{\sigma}}\right)^{n_k} \left(\frac{d_{ss}}{d_0}\right)^{\alpha n_k} \exp\left[-\frac{Q_k}{R}\left(\frac{1}{T} - \frac{1}{\bar{T}_k}\right)\right]. \tag{B2}$$

There is no closed-form solution either, so we proceed with a numerical solution. We then calculate the new stress caused by the new velocity V_2, which satisfies

$$V_2 = \sum_{k=1}^{M} V_0 \left(\frac{\tau_2}{c_0 + \mu_0 \bar{\sigma}}\right)^{n_k} \left(\frac{d_{ss}}{d_0}\right)^{\alpha n_k} \exp\left[-\frac{Q_k}{R}\left(\frac{1}{T} - \frac{1}{\bar{T}_k}\right)\right], \tag{B3}$$

with the same micro-asperity size. Finally, we simulate the relaxation to a new steady state as an initial-value problem. Using the evolution law generalizing the aging law, the evolutionary phase is governed by the following equations

$$\begin{aligned} \frac{\dot{d}}{d} &= \sum_{k=1}^{N} \frac{G_k}{p_k d^{p_k}} \exp\left[-\frac{H_k}{R}\left(\frac{1}{T} - \frac{1}{T_k}\right)\right] - \frac{\lambda V}{2h}, \\ \frac{\dot{\tau}}{\tau} &= \frac{m}{n}\frac{\dot{d}}{d} - \frac{Q}{nRT}\frac{\dot{T}}{T} \end{aligned} \tag{B4}$$

where, n, Q, and m are defined in Equations A6–A8, respectively. Using the evolution law that generalizes the slip law, the system obeys

$$\begin{aligned} \frac{\dot{d}}{d} &= \frac{\lambda V}{2h} \ln\left\{\frac{2h}{\lambda V} \sum_{k=1}^{N} \frac{G_k}{p_k d^{p_k}} \exp\left[-\frac{H_k}{R}\left(\frac{1}{T} - \frac{1}{T_k}\right)\right]\right\} \\ \frac{\dot{\tau}}{\tau} &= \frac{m}{n}\frac{\dot{d}}{d} - \frac{Q}{nRT}\frac{\dot{T}}{T}. \end{aligned} \tag{B5}$$

The evolution of temperature is solved using the membrane diffusion as in Appendix C, but can be neglected because of the micro-meter scale of slip during laboratory experiments. We solve the coupled ordinary differential equations using a fifth-order accurate Runge-Kutta method with adaptive time steps (Press et al., 1992). Example numerical simulations are shown in Figures 6c and 6d showing the temperature-dependence of $a - b$ due to the competition between healing mechanisms followed by an increase in a due to the activation of a second deformation mechanism. Another application is shown for basalt friction in Figures 11e and 11f.

Appendix C: Numerical Simulations of Seismic Cycles

We conduct seismic cycle simulations for a spring-slider assembly assuming the radiation-damping and membrane diffusion approximations (Rice, 2006; Rice & Tse, 1986; Rice et al., 2001; Segall et al., 2010; Tse & Rice, 1986; L. Wang & Barbot, 2020). The system is loaded at a constant velocity V_L. The constitutive law of Equation 4 provides

$$\frac{\dot{\tau}}{\tau} = \frac{1}{n}\frac{\dot{V}}{V} + \frac{m}{n}\frac{\dot{d}}{d} - \frac{Q}{nRT}\frac{\dot{T}}{T} \tag{C1}$$

where, n, Q, and m are defined in Equations A6–A8, respectively. The conservation of momentum with the radiation-damping approximation provides

$$\dot{\tau} = -k(V - V_L) - \frac{G}{2V_s}\dot{V} \tag{C2}$$

where $V_L = 1$ nm/s is the imposed loading rate, k is the spring stiffness, and V_s is the shear wave speed. Equations C1 and C2 provide the slip acceleration and the evolution of asperity size is provided by Equation 7 or Equation 8. Considering the competition between shear heating and temperature diffusion within the membrane diffusion approximation, the conservation of energy equation becomes

$$\dot{T} = -\frac{D}{W^2}(T - T_b) + \frac{\tau V}{\rho c h}, \tag{C3}$$

where $D = 10^{-6}$ m^2/s is the thermal diffusivity, $W = 4$ cm is the characteristic width of diffusion, and $\rho c = 3$ MPa/K is the volume heat capacity. We solve the coupled ordinary differential equations using a fifth-order accurate Runge-Kutta method with adaptive time steps. Example simulations can be found in Figure 6b. The additional parameters are shown in Table 1. With the choice of parameters, the change of temperature from shear heating does not measurably change the frictional properties.

Conflict of Interest

The authors declare no conflicts of interest relevant to this study.

Data Availability Statement

All data used in this article are available in the published manuscripts, including dry powdered albite gouge (Nakatani, 2001), wet Westerly granite gouge (Blanpied et al., 1995, 1998), Alpine Fault gouge (Niemeijer et al., 2016), and basalt gouge (Okuda et al., 2023). The time series in Figures 11c and 11d are available in the Yoda data repository https://public.yoda.uu.nl/geo/UU01/Q0VVEX.html. The scripts generating Figures 1–11 and the associated curated data are available on zenodo (https://doi.org/10.5281/zenodo.8266306) (Barbot, 2023).

Acknowledgments
We thank Eric Dunham and Norman Sleep for their insightful reviews. We acknowledge funding from the National Science Foundation, under award number EAR-1848192.

References

Acosta, M., Passelègue, F., Schubnel, A., & Violay, M. (2018). Dynamic weakening during earthquakes controlled by fluid thermodynamics. *Nature Communications*, *9*(1), 1–9. https://doi.org/10.1038/s41467-018-05603-9

Aharonov, E., & Scholz, C. H. (2018). A physics-based rock friction constitutive law: Steady state friction. *Journal of Geophysical Research*, *123*(2), 1591–1614. https://doi.org/10.1002/2016jb013829

Aharonov, E., & Scholz, C. H. (2019). The brittle-ductile transition predicted by a physics-based friction law. *Journal of Geophysical Research*, *124*(3), 2721–2737. https://doi.org/10.1029/2018JB016878

An, M., Zhang, F., Elsworth, D., Xu, Z., Chen, Z., & Zhang, L. (2020). Friction of Longmaxi shale gouges and implications for seismicity during hydraulic fracturing. *Journal of Geophysical Research*, *125*(8), e2020JB019885. https://doi.org/10.1029/2020JB019885

Archard, J. F. (1957). Elastic deformation and the laws of friction. *Proceedings of the Royal Society of London A*, *243*(1233), 190–205. https://doi.org/10.1098/rspa.1957.0214

Atkinson, B. K. (1984). Subcritical crack growth in geological materials. *Journal of Geophysical Research*, *89*(B6), 4077–4114. https://doi.org/10.1029/jb089ib06p04077

Barbot, S. (2018). Asthenosphere flow modulated by megathrust earthquake cycles. *Geophysical Research Letters*, *45*(12), 6018–6031. https://doi.org/10.1029/2018GL078197

Barbot, S. (2019a). Slow-slip, slow earthquakes, period-two cycles, full and partial ruptures, and deterministic chaos in a single asperity fault. *Tectonophysics*, *768*, 228171. https://doi.org/10.1016/j.tecto.2019.228171

Barbot, S. (2019b). Modulation of fault strength during the seismic cycle by grain-size evolution around contact junctions. *Tectonophysics*, *765*, 129–145. https://doi.org/10.1016/j.tecto.2019.05.004

Barbot, S. (2020a). Frictional and structural controls of seismic super-cycles at the Japan trench. *Earth Planets and Space*, *72*(63), 63. https://doi.org/10.1186/s40623-020-01185-3

Barbot, S. (2020b). Mantle flow distribution beneath the California margin. *Nature Communications*, *11*(1), 1–14. https://doi.org/10.1038/s41467-020-18260-8

Barbot, S. (2022). A rate-state-and temperature-dependent friction law with competing healing mechanisms. *Journal of Geophysical Research*, *127*(11), e2022JB025106. https://doi.org/10.1029/2022JB025106

Barbot, S. (2023). Constitutive behavior of rocks during the seismic cycle. https://doi.org/10.5281/zenodo.8266306

Barbot, S., Lapusta, N., & Avouac, J. P. (2012). Under the hood of the earthquake machine: Towards predictive modeling of the seismic cycle. *Science*, *336*(6082), 707–710. https://doi.org/10.1126/science.1218796

Barbot, S., Luo, H., Wang, T., Hamiel, Y., Piatibratova, O., Javed, M. T., et al. (2023). Slip distribution of the february 6, 2023 Mw 7.8 and Mw 7.6, Kahramanmaraş, Turkey earthquake sequence in the East Anatolian fault zone. *Seismica*, *2*(3). https://doi.org/10.26443/seismica.v2i3.502

Bar-Sinai, Y., Spatschek, R., Brener, E. A., & Bouchbinder, E. (2014). On the velocity-strengthening behavior of dry friction. *Journal of Geophysical Research*, *119*(3), 1738–1748. https://doi.org/10.1002/2013JB010586

Bayart, E., Svetlizky, I., & Fineberg, J. (2018). Rupture dynamics of heterogeneous frictional interfaces. *Journal of Geophysical Research*, *123*(5), 3828–3848. https://doi.org/10.1002/2018JB015509

Bedford, J. D., Faulkner, D. R., Allen, M. J., & Hirose, T. (2021). The stabilizing effect of high pore-fluid pressure along subduction megathrust faults: Evidence from friction experiments on accretionary sediments from the Nankai Trough. *Earth and Planetary Science Letters*, *574*, 117161. https://doi.org/10.1016/j.epsl.2021.117161

Ben-David, O., & Fineberg, J. (2011). Static friction coefficient is not a material constant. *Physical Review Letters*, *106*(25), 254301. https://doi.org/10.1103/PhysRevLett.106.254301

Ben-David, O., Rubinstein, S. M., & Fineberg, J. (2010). Slip-stick and the evolution of frictional strength. *Nature*, *463*(7277), 76–79. https://doi.org/10.1038/nature08676

Bergsaker, A. S., Røyne, A., Ougier-Simonin, A., Aubry, J., & Renard, F. (2016). The effect of fluid composition, salinity, and acidity on subcritical crack growth in calcite crystals. *Journal of Geophysical Research*, *121*(3), 1631–1651. https://doi.org/10.1002/2015JB012723

Bernabé, Y., & Pec, M. (2022). Brittle creep and failure: A reformulation of the wing crack model. *Journal of Geophysical Research*, *127*(9), e2022JB024610. https://doi.org/10.1029/2022JB024610

Blanpied, M. L., Lockner, D. A., & Byerlee, J. D. (1995). Frictional slip of granite at hydrothermal conditions. *Journal of Geophysical Research*, *100*(B7), 13045–13064. https://doi.org/10.1029/95JB00862

Blanpied, M. L., Marone, C., Lockner, D., Byerlee, J., & King, D. (1998). Quantitative measure of the variation in fault rheology due to fluid-rock interactions. *Journal of Geophysical Research*, *103*(B5), 9691–9712. https://doi.org/10.1029/98JB00162

Boitnott, G., Biegel, R., Scholz, C., Yoshioka, N., & Wang, W. (1992). Micromechanics of rock friction 2: Quantitative modeling of initial friction with contact theory. *Journal of Geophysical Research*, *97*(B6), 8965–8978. https://doi.org/10.1029/92JB00019

Boulton, C., Barth, N. C., Moore, D. E., Lockner, D. A., Townend, J., & Faulkner, D. R. (2018). Frictional properties and 3-D stress analysis of the southern Alpine Fault, New Zealand. *Journal of Structural Geology*, *114*, 43–54. https://doi.org/10.1016/j.jsg.2018.06.003

Boulton, C., Moore, D. E., Lockner, D. A., Toy, V. G., Townend, J., & Sutherland, R. (2014). Frictional properties of exhumed fault gouges in DFDP-1 cores, Alpine Fault, New Zealand. *Geophysical Research Letters*, *41*(2), 356–362. https://doi.org/10.1002/2013GL058236

Bowden, F. P., & Tabor, D. (1950). *The friction and lubrication of Solids, Part I*. Clarendon Press.

Bowden, F. P., & Tabor, D. (1964). *The friction and lubrication of Solids, Part II*. Clarendon Press.

Brantut, N., Passelègue, F. X., Deldicque, D., Rouzaud, J.-N., & Schubnel, A. (2016). Dynamic weakening and amorphization in serpentinite during laboratory earthquakes. *Geology*, *44*(8), 607–610. https://doi.org/10.1130/G37932.1

Brechet, Y., & Estrin, Y. (1994). The effect of strain rate sensitivity on dynamic friction of metals. *Scripta Metallurgica et Materialia*, *30*(11), 1449–1454. https://doi.org/10.1016/0956-716X(94)90244-5

Brenguier, F., Campillo, M., Hadziioannou, C., Shapiro, N. M., Nadeau, R. M., & Larose, E. (2008). Postseismic relaxation along the San Andreas fault at Parkfield from continuous seismological observations. *Science*, *321*(5895), 1478–1481. https://doi.org/10.1126/science.1160943

Brown, K. M., & Fialko, Y. (2012). 'Melt welt' mechanism of extreme weakening of gabbro at seismic slip rates. *Nature*, *488*(7413), 638–641. https://doi.org/10.1038/nature11370

Bureau, L., Baumberger, T., & Caroli, C. (2002). Rheological aging and rejuvenation in solid friction contacts. *The European Physical Journal E*, *8*(3), 331–337. https://doi.org/10.1140/epje/i2002-10017-1

Bürgmann, R., & Dresen, G. (2008). Rheology of the lower crust and upper mantle: Evidence from rock mechanics, geodesy, and field observations. *Annual Review of Earth and Planetary Sciences*, *36*(1), 531–567. https://doi.org/10.1146/annurev.earth.36.031207.124326

Byerlee, J. (1978). Friction of rock. *Pure and Applied Geophysics*, *116*(4–5), 615–626. https://doi.org/10.1007/bf00876528

Carpenter, B., Collettini, C., Viti, C., & Cavallo, A. (2016). The influence of normal stress and sliding velocity on the frictional behaviour of calcite at room temperature: Insights from laboratory experiments and microstructural observations. *Geophysical Journal International*, *205*(1), 548–561. https://doi.org/10.1093/gji/ggw038

Carpenter, B., Ikari, M., & Marone, C. (2016). Laboratory observations of time-dependent frictional strengthening and stress relaxation in natural and synthetic fault gouges. *Journal of Geophysical Research*, *121*(2), 1183–1201. https://doi.org/10.1002/2015jb012136

Cebry, S. B. L., Ke, C.-Y., Shreedharan, S., Marone, C., Kammer, D. S., & McLaskey, G. C. (2022). Creep fronts and complexity in laboratory earthquake sequences illuminate delayed earthquake triggering. *Nature Communications*, *13*(1), 6839. https://doi.org/10.1038/s41467-022-34397-0

Charles, R. (1958). Dynamic fatigue of glass. *Journal of Applied Physics*, *29*(12), 1657–1662. https://doi.org/10.1063/1.1723019

Chen, J. (2023). The emergence of four types of slow slip cycles on dilatant, fluid saturated faults. *Journal of Geophysical Research*, *128*(2), e2022JB024382. https://doi.org/10.1029/2022JB024382

Chen, J., Niemeijer, A., & Spiers, C. J. (2017). Microphysically derived expressions for rate-and-state friction parameters, a, b, and Dc. *Journal of Geophysical Research*, *122*(12), 9627–9657. https://doi.org/10.1002/2017JB014226

Chen, J., Niemeijer, A., & Spiers, C. J. (2021). Microphysical modeling of carbonate fault friction at slip rates spanning the full seismic cycle. *Journal of Geophysical Research*, *126*(3), e2020JB021024. https://doi.org/10.1029/2020jb021024

Chen, J., & Spiers, C. J. (2016). Rate and state frictional and healing behavior of carbonate fault gouge explained using microphysical model. *Journal of Geophysical Research*, *121*(12), 8642–8665. https://doi.org/10.1002/2016jb013470

Chen, J., Verberne, B., & Niemeijer, A. (2020). Flow-to-friction transition in simulated calcite gouge: Experiments and microphysical modeling. *Journal of Geophysical Research*, *125*(11), e2020JB019970. https://doi.org/10.1029/2020JB019970

Chen, T., & Lapusta, N. (2009). Scaling of small repeating earthquakes explained by interaction of seismic and aseismic slip in a rate and state fault model. *Journal of Geophysical Research*, *114*(B01311), 12. https://doi.org/10.1029/2008jb005749

Chester, F. M. (1994). Effects of temperature on friction: Constitutive equations and experiments with fault gouge. *Journal of Geophysical Research*, *99*(B4), 7247–7261. https://doi.org/10.1029/93JB03110

Chester, F. M. (1995). A rheologic model for wet crust applied to strike-slip faults. *Journal of Geophysical Research*, *100*(B7), 13033–13044. https://doi.org/10.1029/95JB00313

Chester, F. M., & Higgs, N. (1992). Multimechanism friction constitutive model for ultrafine quartz gouge at hypocentral conditions. *Journal of Geophysical Research*, *97*(B2), 1859–1870. https://doi.org/10.1029/91JB02349

Chevoir, F., Roux, J.-N., da Cruz, F., Rognon, P. G., & Koval, G., Jr. (2009). Friction law in dense granular flows. *Powder Technology*, *190*(1–2), 264–268. https://doi.org/10.1016/j.powtec.2008.04.061

Coble, C., French, M., Chester, F., Chester, J., & Kitajima, H. (2014). In situ frictional properties of San Andreas Fault gouge at SAFOD. *Geophysical Journal International*, *199*(2), 956–967. https://doi.org/10.1093/gji/ggu306

Collettini, C., Niemeijer, A., Viti, C., Smith, S. A., & Marone, C. (2011). Fault structure, frictional properties and mixed-mode fault slip behavior. *Earth and Planetary Science Letters*, *311*(3), 316–327. https://doi.org/10.1016/j.epsl.2011.09.020

Collettini, C., Tesei, T., Scuderi, M. M., Carpenter, B. M., & Viti, C. (2019). Beyond Byerlee friction, weak faults and implications for slip behavior. *Earth and Planetary Science Letters*, *519*, 245–263. https://doi.org/10.1016/j.epsl.2019.05.011

Conrad, E., Tisato, N., Carpenter, B., & Di Toro, G. (2023). Influence of frictional melt on the seismic cycle: Insights from experiments on rock analog material. *Journal of Geophysical Research*, *128*(1), e2022JB025695. https://doi.org/10.1029/2022JB025695

Cornelio, C., Spagnuolo, E., Di Toro, G., Nielsen, S., & Violay, M. (2019). Mechanical behaviour of fluid-lubricated faults. *Nature Communications*, *10*(1), 1–7. https://doi.org/10.1038/s41467-019-09293-9

Coulomb, C. A. (1821). *Théorie des machines simples, en ayant égard au frottement de leurs parties et à la roideur des cordages*. Bachelier.

Cox, S., & Paterson, M. (1991). Experimental dissolution-precipitation creep in quartz aggregates at high temperatures. *Geophysical Research Letters*, *18*(8), 1401–1404. https://doi.org/10.1029/91GL01802

Davis, G. H., Bump, A. P., Garcıa, P. E., & Ahlgren, S. G. (2000). Conjugate Riedel deformation band shear zones. *Journal of Structural Geology*, *22*(2), 169–190. https://doi.org/10.1016/S0191-8141(99)00140-6

den Hartog, S., Niemeijer, A., & Spiers, C. J. (2012). New constraints on megathrust slip stability under subduction zone P–T conditions. *Earth and Planetary Science Letters*, *353*, 240–252. https://doi.org/10.1016/j.epsl.2012.08.022

den Hartog, S., Thomas, M. Y., & Faulkner, D. (2021). How do laboratory friction parameters compare with observed fault slip and geodetically derived friction parameters? Insights from the Longitudinal Valley Fault, Taiwan. *Journal of Geophysical Research*, *126*(10), e2021JB022390. https://doi.org/10.1029/2021JB022390

Dieterich, J. H. (1972). Time-dependent friction in rocks. *Journal of Geophysical Research*, *77*(20), 3690–3697. https://doi.org/10.1029/JB077i020p03690

Dieterich, J. H. (1978). Time-dependent friction and the mechanics of stick-slip. *Pure and Applied Geophysics*, *116*(4–5), 790–806. https://doi.org/10.1007/978-3-0348-7182-2_15

Dieterich, J. H. (1979). Modeling of rock friction 1. Experimental results and constitutive equations. *Journal of Geophysical Research*, *84*(B5), 2161–2168. https://doi.org/10.1029/JB084iB05p02161

Dieterich, J. H. (1981). Constitutive properties of faults with simulated gouge. In J. M. L. N. L. Carter, M. Friedman, & D. W. Stearns (Eds.) *Monograph 24: Mechanical behavior of crustal rocks* (pp. 103–120). AGU. https://doi.org/10.1029/GM024p0103

Dieterich, J. H., & Conrad, G. (1984). Effect of humidity on time-and velocity-dependent friction in rocks. *Journal of Geophysical Research*, *89*(B6), 4196–4202. https://doi.org/10.1029/JB089iB06p04196

Dieterich, J. H., & Kilgore, B. D. (1994). Direct observation of frictional contacts: New insights for sliding memory effects. *Pure and Applied Geophysics*, *143*(1–3), 283–302. https://doi.org/10.1007/BF00874332

Dieterich, J. H., & Kilgore, B. D. (1996). Imaging surface contacts: Power law contact distributions and contact stresses in quartz, calcite, glass and acrylic plastic. *Tectonophysics*, *256*(1–4), 219–239. https://doi.org/10.1016/0040-1951(95)00165-4

Di Toro, G., Goldsby, D. L., & Tullis, T. E. (2004). Friction falls towards zero in quartz rock as slip velocity approaches seismic rates. *Nature*, *427*(6973), 436–439. https://doi.org/10.1038/nature02249

Di Toro, G., Hirose, T., Nielsen, S., Pennacchioni, G., & Shimamoto, T. (2006). Natural and experimental evidence of melt lubrication of faults during earthquakes. *Science*, *311*(5761), 647–649. https://doi.org/10.1126/science.1121012

Di Toro, G., Pennacchioni, G., & Teza, G. (2005). Can pseudotachylytes be used to infer earthquake source parameters? An example of limitations in the study of exhumed faults. *Tectonophysics*, *402*(1–4), 3–20. https://doi.org/10.1016/j.tecto.2004.10.014

Dunning, J., Douglas, B., Miller, M., & McDonald, S. (1994). The role of the chemical environment in frictional deformation: Stress corrosion cracking and comminution. *Pure and Applied Geophysics*, *143*(1), 151–178. https://doi.org/10.1007/BF00874327

Engelder, J., & Scholz, C. (1976). The role of asperity indentation and ploughing in rock friction—II: Influence of relative hardness and normal load. In *International Journal of rock mechanics and mining sciences and geomechanics abstracts* (Vol. 13, pp. 155–163). Elsevier. https://doi.org/10.1016/0148-9062(76)90820-2

Fialko, Y., Sandwell, D., Simons, M., & Rosen, P. (2005). Three-dimensional deformation caused by the Bam, Iran, earthquake and the origin of shallow slip deficit. *Nature*, *435*(7040), 295–299. https://doi.org/10.1038/nature03425

Frost, H., & Ashby, M. (1982). *Deformation-mechanism maps: The plasticity and creep of metals and ceramics*. Franklin Book Company, Incorporated.

Frye, K. M., & Marone, C. (2002). Effect of humidity on granular friction at room temperature. *Journal of Geophysical Research*, *107*(B11), ETG-11–ETG11-13. https://doi.org/10.1029/2001JB000654

Fukuyama, E., Yamashita, F., & Mizoguchi, K. (2019). Voids and rock friction at subseismic slip velocity. In *Earthquakes and multi-hazards around the Pacific Rim* (Vol. II, pp. 87–107). Springer.

Gauriau, J., Barbot, S., & Dolan, J. F. (2023). Islands of chaos in a sea of periodic earthquakes. *Earth and Planetary Science Letters*, *618*, 118274. https://doi.org/10.1016/j.epsl.2023.118274

Goebel, T., Candela, T., Sammis, C., Becker, T., Dresen, G., & Schorlemmer, D. (2014). Seismic event distributions and off-fault damage during frictional sliding of saw-cut surfaces with pre-defined roughness. *Geophysical Journal International*, *196*(1), 612–625. https://doi.org/10.1093/gji/ggu074

Goswami, A., & Barbot, S. (2018). Slow-slip events in semi-brittle serpentinite fault zones. *Scientific Reports*, *8*(1), 6181. https://doi.org/10.1038/s41598-018-24637-z

Gratier, J.-P., Guiguet, R., Renard, F., Jenatton, L., & Bernard, D. (2009). A pressure solution creep law for quartz from indentation experiments. *Journal of Geophysical Research*, *114*(B3), B03403. https://doi.org/10.1029/2008JB005652

Greenwood, J. A., & Williamson, J. (1966). Contact of nominally flat surfaces. *Proceedings of the Royal Society of London Series A*, *295*(1442), 300–319. https://doi.org/10.1098/rspa.1966.0242

Haines, S., Marone, C., & Saffer, D. (2014). Frictional properties of low-angle normal fault gouges and implications for low-angle normal fault slip. *Earth and Planetary Science Letters*, *408*, 57–65. https://doi.org/10.1016/j.epsl.2014.09.034

Hall, C. E., & Parmentier, E. (2003). Influence of grain size evolution on convective instability. *Geochemistry, Geophysics, Geosystems*, *4*(3), 353. https://doi.org/10.1029/2002gc000308

Hansen, L., Zimmerman, M., & Kohlstedt, D. L. (2011). Grain boundary sliding in San Carlos olivine: Flow law parameters and crystallographic-preferred orientation. *Journal of Geophysical Research*, *116*(B8), B08201. https://doi.org/10.1029/2011JB008220

He, C., Luo, L., Hao, Q.-M., & Zhou, Y. (2013). Velocity-weakening behavior of plagioclase and pyroxene gouges and stabilizing effect of small amounts of quartz under hydrothermal conditions. *Journal of Geophysical Research*, *118*(7), 3408–3430. https://doi.org/10.1002/jgrb.50280

He, C., Tan, W., & Zhang, L. (2016). Comparing dry and wet friction of plagioclase: Implication to the mechanism of frictional evolution effect at hydrothermal conditions. *Journal of Geophysical Research*, *121*(9), 6365–6383. https://doi.org/10.1002/2016JB012834

He, C., Wang, Z., & Yao, W. (2007). Frictional sliding of gabbro gouge under hydrothermal conditions. *Tectonophysics*, *445*(3–4), 353–362. https://doi.org/10.1016/j.tecto.2007.09.008

He, C., Yao, W., Wang, Z., & Zhou, Y. (2006). Strength and stability of frictional sliding of gabbro gouge at elevated temperatures. *Tectonophysics*, *427*(1–4), 217–229. https://doi.org/10.1016/j.tecto.2006.05.023

Heslot, F., Baumberger, T., Perrin, B., Caroli, B., & Caroli, C. (1994). Creep, stick-slip, and dry friction dynamics: Experiments and a heuristic model. *Physical Review E*, *49*(6), 4973–4988. https://doi.org/10.1103/physreve.49.4973

Higgs, N. G. (1981). *Mechanical properties of ultrafine quartz, chlorite and bentonite in environments appropriate to upper-crustal earthquakes* (p. 267). Texas A &M University.

Hirauchi, K.-I., Hibi, R., Shirahige, R., & Takemura, T. (2023). Effects of phyllosilicate content on the slip behavior of fault gouge: Insights from room-temperature friction experiments on quartz–talc mixtures. *Tectonophysics*, *857*, 229845. https://doi.org/10.1016/j.tecto.2023.229845

Hirth, G., & Kohlstedt, D. L. (2003). Rheology of the upper mantle and the mantle wedge: A view from the experimentalists. In J. Eiler (Ed.) *Inside the subduction factory, geophysical monograph* (Vol. 138, pp. 83–105). American Geophysical Society. https://doi.org/10.1029/138GM06

Hussain, E., Wright, T. J., Walters, R. J., Bekaert, D., Hooper, A., & Houseman, G. A. (2016). Geodetic observations of postseismic creep in the decade after the 1999 Izmit earthquake, Turkey: Implications for a shallow slip deficit. *Journal of Geophysical Research*, *121*(4), 2980–3001. https://doi.org/10.1002/2015JB012737

Ikari, M. J., Ito, Y., Ujiie, K., & Kopf, A. J. (2015). Spectrum of slip behaviour in Tohoku fault zone samples at plate tectonic slip rates. *Nature Geoscience*, *8*(11), 870–874. https://doi.org/10.1038/ngeo2547

Ikari, M. J., & Kopf, A. J. (2017). Seismic potential of weak, near-surface faults revealed at plate tectonic slip rates. *Science Advances*, *3*(11), e1701269. https://doi.org/10.1126/sciadv.1701269

Ikari, M. J., & Saffer, D. M. (2011). Comparison of frictional strength and velocity dependence between fault zones in the Nankai accretionary complex. *Geochemistry, Geophysics, Geosystems*, *12*(4), Q0AD16. https://doi.org/10.1029/2010GC003442

Ikari, M. J., Trütner, S., Carpenter, B. M., & Kopf, A. J. (2015). Shear behavior of DFDP-1 borehole samples from the Alpine Fault, New Zealand, under a wide range of experimental conditions. *International Journal of Earth Sciences*, *104*(6), 1523–1535. https://doi.org/10.1007/s00531-014-1115-5

Im, K., Elsworth, D., & Wang, C. (2019). Cyclic permeability evolution during repose then reactivation of fractures and faults. *Journal of Geophysical Research*, *124*(5), 4492–4506. https://doi.org/10.1029/2019JB017309

Im, K., Saffer, D., Marone, C., & Avouac, J.-P. (2020). Slip-rate-dependent friction as a universal mechanism for slow slip events. *Nature Geoscience*, *13*(10), 705–710. https://doi.org/10.1038/s41561-020-0627-9

Ito, Y., Obara, K., Shiomi, K., Sekine, S., & Hirose, H. (2007). Slow earthquakes coincident with episodic tremors and slow slip events. *Science*, *315*(5811), 503–506. https://doi.org/10.1126/science.1134454

Kanagawa, K., Cox, S. F., & Zhang, S. (2000). Effects of dissolution-precipitation processes on the strength and mechanical behavior of quartz gouge at high-temperature hydrothermal conditions. *Journal of Geophysical Research*, *105*(B5), 11115–11126. https://doi.org/10.1029/2000JB900038

Kaneko, Y., Avouac, J.-P., & Lapusta, N. (2010). Towards inferring earthquake patterns from geodetic observations of interseismic coupling. *Nature Geoscience*, *3*(5), 363–369. https://doi.org/10.1038/ngeo843

Kaneko, Y., Nielsen, S. B., & Carpenter, B. M. (2016). The onset of laboratory earthquakes explained by nucleating rupture on a rate-and-state fault. *Journal of Geophysical Research*, *121*(8), 6071–6091. https://doi.org/10.1002/2016jb013143

Kaproth, B. M., & Marone, C. (2013). Slow earthquakes, preseismic velocity changes, and the origin of slow frictional stick-slip. *Science*, *341*(6151), 1229–1232. https://doi.org/10.1126/science.1239577

Karato, S.-I. (2008). *Deformation of Earth materials: An introduction to the rheology of solid Earth*. Cambridge University Press.

Karato, S.-I., & Jung, H. (2003). Effects of pressure on high-temperature dislocation creep in olivine. *Philosophical Magazine*, *83*(3), 401–414. https://doi.org/10.1080/0141861021000025829

Kato, A., & Ben-Zion, Y. (2021). The generation of large earthquakes. *Nature Reviews Earth and Environment*, *2*(1), 26–39. https://doi.org/10.1038/s43017-020-00108-w

Kilgore, B. D., Blanpied, M. L., & Dieterich, J. H. (1993). Velocity dependent friction of granite over a wide range of conditions. *Geophysical Research Letters*, *20*(10), 903–906. https://doi.org/10.1029/93GL00368

Kirkpatrick, J. D., Dobson, K. J., Mark, D., Shipton, Z., Brodsky, E., & Stuart, F. (2012). The depth of pseudotachylyte formation from detailed thermochronology and constraints on coseismic stress drop variability. *Journal of Geophysical Research*, *117*(B6), 6406. https://doi.org/10.1029/2011jb008846

Kocharyan, G. G., Ostapchuk, A. A., & Pavlov, D. V. (2018). Traces of laboratory earthquake nucleation in the spectrum of ambient noise. *Scientific Reports*, *8*(1), 10764. https://doi.org/10.1038/s41598-018-28976-9

Kohli, A., Wolfson-Schwehr, M., Prigent, C., & Warren, J. M. (2021). Oceanic transform fault seismicity and slip mode influenced by seawater infiltration. *Nature Geoscience*, *14*(8), 606–611. https://doi.org/10.1038/s41561-021-00778-1

Kohli, A. H., & Zoback, M. D. (2013). Frictional properties of shale reservoir rocks. *Journal of Geophysical Research*, *118*(9), 5109–5125. https://doi.org/10.1002/jgrb.50346

Kubo, T., & Katayama, I. (2015). Effect of temperature on the frictional behavior of smectite and illite. *Journal of Mineralogical and Petrological Sciences*, *110*(6), 293–299. https://doi.org/10.2465/jmps.150421

Kuna, V. M., Nábělek, J. L., & Braunmiller, J. (2019). Mode of slip and crust–mantle interaction at oceanic transform faults. *Nature Geoscience*, *12*(2), 138–142. https://doi.org/10.1038/s41561-018-0287-1

Lapusta, N., & Rice, J. R. (2003). Nucleation and early seismic propagation of small and large events in a crustal earthquake model. *Journal of Geophysical Research*, *108*(B4), 2205. https://doi.org/10.1029/2001JB000793

Lapusta, N., Rice, J. R., BenZion, Y., & Zheng, G. (2000). Elastodynamics analysis for slow tectonic loading with spontaneous rupture episodes on faults with rate- and state-dependent friction. *Journal of Geophysical Research*, *105*(B10), 23765–23789. https://doi.org/10.1029/2000jb900250

Leeman, J., Saffer, D., Scuderi, M., & Marone, C. (2016). Laboratory observations of slow earthquakes and the spectrum of tectonic fault slip modes. *Nature Communications*, *7*(1), 11104. https://doi.org/10.1038/ncomms11104

Leu, D.-K. (2009). A simple dry friction model for metal forming process. *Journal of Materials Processing Technology*, *209*(5), 2361–2368. https://doi.org/10.1016/j.jmatprotec.2008.05.027

Li, D., & Liu, Y. (2017). Modeling slow-slip segmentation in cascadia subduction zone constrained by tremor locations and gravity anomalies. *Journal of Geophysical Research*, *122*(4), 3138–3157. https://doi.org/10.1002/2016JB013778

Li, Y., Vidale, J., Aki, K., Xu, F., & Burdette, T. (1998). Evidence of shallow fault zone strengthening after the 1992 M7.5 Landers, California, earthquake. *Science*, *279*(5348), 217–219. https://doi.org/10.1126/science.279.5348.217

Liang, C., Ampuero, J.-P., & Pino Muñoz, D. (2022). The paucity of supershear earthquakes on large faults governed by rate and state friction. *Geophysical Research Letters*, *49*(22), e2022GL099749. https://doi.org/10.1029/2022GL099749
Linker, M. H., & Dieterich, J. H. (1992). Effects of variable normal stress on rock friction: Observations and constitutive relations. *Journal of Geophysical Research*, *97*(B4), 4923–4940. https://doi.org/10.1029/92JB00017
Liu, Y., & He, C. (2020). Friction properties of hornblende and implications for slow-slip events in subduction zones. *Tectonophysics*, *796*, 228644. https://doi.org/10.1016/j.tecto.2020.228644
Liu, Y., McGuire, J. J., & Behn, M. D. (2012). Frictional behavior of oceanic transform faults and its influence on earthquake characteristics. *Journal of Geophysical Research*, *117*(B4), B04315. https://doi.org/10.1029/2011JB009025
Liu, Y., & Rice, J. R. (2005). Aseismic slip transients emerge spontaneously in three-dimensional rate and state modeling of subduction earthquake sequences. *Journal of Geophysical Research*, *110*(B8), B08307. https://doi.org/10.1029/2004JB003424
Lockner, D. A., Morrow, C., Moore, D., & Hickman, S. (2011). Low strength of deep San Andreas fault gouge from SAFOD core. *Nature*, *472*(7341), 82–86. https://doi.org/10.1038/nature09927
Lockner, D. A., Summers, R., & Byerlee, J. (1986). Effects of temperature and sliding rate on frictional strength of granite. In *Friction and faulting* (pp. 445–469). Springer. https://doi.org/10.1007/978-3-0348-6601-9_4
Lu, Z., & He, C. (2014). Frictional behavior of simulated biotite fault gouge under hydrothermal conditions. *Tectonophysics*, *622*, 62–80. https://doi.org/10.1016/j.tecto.2014.03.002
Lu, Z., & He, C. (2018). Friction of foliated fault gouge with a biotite interlayer at hydrothermal conditions. *Tectonophysics*, *740*, 72–92. https://doi.org/10.1016/j.tecto.2018.05.003
Maegawa, S., Itoigawa, F., & Nakamura, T. (2015). Effect of normal load on friction coefficient for sliding contact between rough rubber surface and rigid smooth plane. *Tribology International*, *92*, 335–343. https://doi.org/10.1016/j.triboint.2015.07.014
Marone, C., Raleigh, B. C., & Scholz, C. H. (1990). Frictional behavior and constitutive modeling of simulated fault gouge. *Journal of Geophysical Research*, *95*(B5), 7007–7026. https://doi.org/10.1029/JB095iB05p07007
Masuti, S., & Barbot, S. (2021). MCMC inversion of the transient and steady-state creep flow law parameters of dunite under dry and wet conditions. *Earth Planets and Space*, *73*(1), 1–21. https://doi.org/10.1186/s40623-021-01543-9
Masuti, S., Barbot, S., Karato, S., Feng, L., & Banerjee, P. (2016). Upper mantle water stratification inferred from the 2012 Mw 8.6 Indian Ocean earthquake. *Nature*, *538*(7625), 373–377. https://doi.org/10.1038/nature19783
Mergel, J. C., Sahli, R., Scheibert, J., & Sauer, R. A. (2019). Continuum contact models for coupled adhesion and friction. *The Journal of Adhesion*, *95*(12), 1101–1133. https://doi.org/10.1080/00218464.2018.1479258
Michel, S., Avouac, J.-P., Lapusta, N., & Jiang, J. (2017). Pulse-like partial ruptures and high-frequency radiation at creeping-locked transition during megathrust earthquakes. *Geophysical Research Letters*, *44*(16), 8345–8351. https://doi.org/10.1002/2017GL074725
MiDi, G. (2004). On dense granular flows. *The European Physical Journal E*, *14*(4), 341–365. https://doi.org/10.1140/epje/i2003-10153-0
Mitchell, E., Fialko, Y., & Brown, K. (2016). Velocity-weakening behavior of Westerly granite at temperature up to 600°C. *Journal of Geophysical Research*, *121*(9), 6932–6946. https://doi.org/10.1002/2016JB013081
Molinari, A., & Perfettini, H. (2019). Fundamental aspects of a new micromechanical model of rate and state friction. *Journal of the Mechanics and Physics of Solids*, *124*, 63–82. https://doi.org/10.1016/j.jmps.2018.10.002
Moore, D. E., Lockner, D. A., & Hickman, S. (2016). Hydrothermal frictional strengths of rock and mineral samples relevant to the creeping section of the San Andreas Fault. *Journal of Structural Geology*, *89*, 153–167. https://doi.org/10.1016/j.jsg.2016.06.005
Nagata, K., Nakatani, M., & Yoshida, S. (2008). Monitoring frictional strength with acoustic wave transmission. *Geophysical Research Letters*, *35*(6), L06310. https://doi.org/10.1029/2007gl033146
Nagata, K., Nakatani, M., & Yoshida, S. (2012). A revised rate-and state-dependent friction law obtained by constraining constitutive and evolution laws separately with laboratory data. *Journal of Geophysical Research*, *117*(B2), B02314. https://doi.org/10.1029/2011JB008818
Nakatani, M. (2001). Conceptual and physical clarification of rate and state friction: Frictional sliding as a thermally activated rheology. *Journal of Geophysical Research*, *106*(B7), 13347–13380. https://doi.org/10.1029/2000JB900453
Nakatani, M., & Scholz, C. H. (2004). Frictional healing of quartz gouge under hydrothermal conditions: 2. Quantitative interpretation with a physical model. *Journal of Geophysical Research*, *109*(B7), B07202. https://doi.org/10.1029/2003JB002938
Nie, S., & Barbot, S. (2021). Seismogenic and tremorgenic slow slip near the stability transition of frictional sliding. *Earth and Planetary Science Letters*, *569*, 117037. https://doi.org/10.1016/j.epsl.2021.117037
Nie, S., & Barbot, S. (2022). Rupture styles linked to recurrence patterns in seismic cycles with a compliant fault zone. *Earth and Planetary Science Letters*, *591*, 117593. https://doi.org/10.1016/j.epsl.2022.117593
Niemeijer, A. R., Boulton, C., Toy, V., Townend, J., & Sutherland, R. (2016). Large-displacement, hydrothermal frictional properties of DFDP-1 fault rocks, Alpine Fault, New Zealand: Implications for deep rupture propagation. *Journal of Geophysical Research*, *121*(2), 624–647. https://doi.org/10.1002/2015JB012593
Niemeijer, A. R., & Collettini, C. (2014). Frictional properties of a low-angle normal fault under in situ conditions: Thermally-activated velocity weakening. *Pure and Applied Geophysics*, *171*(10), 2641–2664. https://doi.org/10.1007/s00024-013-0759-6
Noda, H., & Lapusta, N. (2013). Stable creeping fault segments can become destructive as a result of dynamic weakening. *Nature*, *493*(7433), 518–521. https://doi.org/10.1038/nature11703
Noda, H., & Shimamoto, T. (2009). Constitutive properties of clayey fault gouge from the Hanaore fault zone, southwest Japan. *Journal of Geophysical Research*, *114*(B4), B04409. https://doi.org/10.1029/2008JB005683
Noda, H., & Shimamoto, T. (2010). A rate- and state-dependent ductile flow law of polycrystalline halite under large shear strain and implications for transition to brittle deformation. *Geophysical Research Letters*, *37*(9), L09310. https://doi.org/10.1029/2010GL042512
Obara, K., & Kato, A. (2016). Connecting slow earthquakes to huge earthquakes. *Science*, *353*(6296), 253–257. https://doi.org/10.1126/science.aaf1512
Okubo, P. G. (1989). Dynamic rupture modeling with laboratory-derived constitutive relations. *Journal of Geophysical Research*, *94*(B9), 12321–12335. https://doi.org/10.1029/jb094ib09p12321
Okuda, H., Niemeijer, A. R., Takahashi, M., Yamaguchi, A., & Spiers, C. J. (2023). Hydrothermal friction experiments on simulated basaltic fault gouge and implications for megathrust earthquakes. *Journal of Geophysical Research*, *128*(1), e2022JB025072. https://doi.org/10.1029/2022JB025072
Pec, M., Stünitz, H., Heilbronner, R., & Drury, M. (2016). Semi-brittle flow of granitoid fault rocks in experiments. *Journal of Geophysical Research*, *121*(3), 1677–1705. https://doi.org/10.1002/2015JB012513
Pec, M., Stünitz, H., Heilbronner, R., Drury, M., & de Capitani, C. (2012). Origin of pseudotachylites in slow creep experiments. *Earth and Planetary Science Letters*, *355*, 299–310. https://doi.org/10.1016/j.epsl.2012.09.004
Poirier, J.-P. (1985). *Creep of crystals: High-temperature deformation processes in metals, ceramics and minerals*. Cambridge University Press.

Popov, V. L., Li, Q., Lyashenko, I. A., & Pohrt, R. (2021). Adhesion and friction in hard and soft contacts: Theory and experiment. *Friction*, *9*(6), 1688–1706. https://doi.org/10.1007/s40544-020-0482-0

Pozzi, G., De Paola, N., Holdsworth, R. E., Bowen, L., Nielsen, S. B., & Dempsey, E. D. (2019). Coseismic ultramylonites: An investigation of nanoscale viscous flow and fault weakening during seismic slip. *Earth and Planetary Science Letters*, *516*, 164–175. https://doi.org/10.1016/j.epsl.2019.03.042

Press, W. H., Teukolsky, S. A., Vetterling, W. T., & Flannery, B. P. (1992). *Numerical recipes in C: The art of scientific computing* (2nd ed., p. 994). Cambridge University Press.

Proctor, B., Lockner, D., Kilgore, B., Mitchell, T., & Beeler, N. (2020). Direct evidence for fluid pressure, dilatancy, and compaction affecting slip in isolated faults. *Geophysical Research Letters*, *47*(16), e2019GL086767. https://doi.org/10.1029/2019GL086767

Qiu, Q., & Barbot, S. (2022). Tsunami excitation in the outer wedge of global subduction zones. *Earth-Science Reviews*, *230*, 104054. https://doi.org/10.1016/j.earscirev.2022.104054

Qiu, Q., Barbot, S., Wang, T., & Wei, S. (2020). Slip complementarity and triggering between the foreshock, mainshock, and afterslip of the 2019 Ridgecrest rupture sequence. *Bulletin of the Seismological Society of America*, *110*(4), 1701–1715. https://doi.org/10.1785/0120200037

Qiu, Q., Hill, E. M., Barbot, S., Hubbard, J., Feng, W., Lindsey, E. O., et al. (2016). The mechanism of partial rupture of a locked megathrust: The role of fault morphology. *Geology*, *44*(10), 875–878. https://doi.org/10.1130/G38178.1

Reches, Z., & Lockner, D. A. (2010). Fault weakening and earthquake instability by powder lubrication. *Nature*, *467*(7314), 452–455. https://doi.org/10.1038/nature09348

Renard, F., Beauprêtre, S., Voisin, C., Zigone, D., Candela, T., Dysthe, D. K., & Gratier, J.-P. (2012). Strength evolution of a reactive frictional interface is controlled by the dynamics of contacts and chemical effects. *Earth and Planetary Science Letters*, *341*, 20–34. https://doi.org/10.1016/j.epsl.2012.04.048

Renard, F., Gratier, J.-P., & Jamtveit, B. (2000). Kinetics of crack-sealing, intergranular pressure solution, and compaction around active faults. *Journal of Structural Geology*, *22*(10), 1395–1407. https://doi.org/10.1016/S0191-8141(00)00064-X

Rice, J. R. (2006). Heating and weakening of faults during earthquake slip. *Journal of Geophysical Research*, *111*(B5), B05311. https://doi.org/10.1029/2005JB004006

Rice, J. R., Lapusta, N., & Ranjith, K. (2001). Rate and state dependent friction and the stability of sliding between elastically deformable solids. *Journal of the Mechanics and Physics of Solids*, *49*(9), 1865–1898. https://doi.org/10.1016/S0022-5096(01)00042-4

Rice, J. R., & Ruina, A. L. (1983). Stability of steady frictional slipping. *Journal of Applied Mechanics*, *50*(2), 343–349. https://doi.org/10.1115/1.3167042

Rice, J. R., & Tse, S. T. (1986). Dynamic motion of a single degree of freedom system following a rate and state dependent friction law. *Journal of Geophysical Research*, *91*(B1), 521–530. https://doi.org/10.1029/jb091ib01p00521

Riedel, W. (1929). *Zur mechanik geologischer Brucherscheinungen (Ein Beitrag zum Problem der Fiederspatten): Centralblatt für Mineralogie*. Geologie und Paläontologie.

Rogers, G., & Dragert, H. (2003). Episodic tremor and slip on the Cascadia subduction zone: The chatter of silent slip. *Science*, *300*(5627), 1942–1943. https://doi.org/10.1126/science.1084783

Rosa, A., El-Barbary, A., Heggie, M., & Briddon, P. (2005). Structural and thermodynamic properties of water related defects in α-quartz. *Physics and Chemistry of Minerals*, *32*(5–6), 323–331. https://doi.org/10.1007/s00269-005-0005-6

Rostom, F., Røyne, A., Dysthe, D. K., & Renard, F. (2013). Effect of fluid salinity on subcritical crack propagation in calcite. *Tectonophysics*, *583*, 68–75. https://doi.org/10.1016/j.tecto.2012.10.023

Rouet-Leduc, B., Hulbert, C., Bolton, D. C., Ren, C. X., Riviere, J., Marone, C., et al. (2018). Estimating fault friction from seismic signals in the laboratory. *Geophysical Research Letters*, *45*(3), 1321–1329. https://doi.org/10.1002/2017gl076708

Rowe, C. D., & Griffith, W. A. (2015). Do faults preserve a record of seismic slip: A second opinion. *Journal of Structural Geology*, *78*, 1–26. https://doi.org/10.1016/j.jsg.2015.06.006

Rowe, C. D., Lamothe, K., Rempe, M., Andrews, M., Mitchell, T. M., Di Toro, G., et al. (2019). Earthquake lubrication and healing explained by amorphous nanosilica. *Nature Communications*, *10*(1), 320. https://doi.org/10.1038/s41467-018-08238-y

Rowe, C. D., Ross, C., Swanson, M. T., Pollock, S., Backeberg, N. R., Barshi, N. A., et al. (2018). Geometric complexity of earthquake rupture surfaces preserved in pseudotachylyte networks. *Journal of Geophysical Research*, *123*(9), 7998–8015. https://doi.org/10.1029/2018JB016192

Rubinstein, S. M., Cohen, G., & Fineberg, J. (2004). Detachment fronts and the onset of dynamic friction. *Nature*, *430*(7003), 1005–1009. https://doi.org/10.1038/nature02830

Ruggieri, R., Scuderi, M. M., Trippetta, F., Tinti, E., Brignoli, M., Mantica, S., et al. (2021). The role of shale content and pore-water saturation on frictional properties of simulated carbonate faults. *Tectonophysics*, *807*, 228811. https://doi.org/10.1016/j.tecto.2021.228811

Ruina, A. (1983). Slip instability and state variable friction laws. *Journal of Geophysical Research*, *88*(B12), 10359–10370. https://doi.org/10.1029/JB088iB12p10359

Sahli, R., Pallares, G., Ducottet, C., Ali, I. B., Al Akhrass, S., Guibert, M., & Scheibert, J. (2018). Evolution of real contact area under shear and the value of static friction of soft materials. *Proceedings of the National Academy of Sciences*, *115*(3), 471–476. https://doi.org/10.1073/pnas.1706434115

Sathiakumar, S., & Barbot, S. (2021). The stop-start control of seismicity by fault bends along the Main Himalayan Thrust. *Communications Earth & Environment*, *2*(1), 1–11. https://doi.org/10.1038/s43247-021-00153-3

Scholz, C., & Engelder, J. (1976). The role of asperity indentation and ploughing in rock friction—I: Asperity creep and stick-slip. In *International Journal of rock mechanics and mining sciences and geomechanics abstracts* (Vol. 13, pp. 149–154). Elsevier. https://doi.org/10.1016/0148-9062(76)90819-6

Schwartz, S. Y., & Rokosky, J. M. (2007). Slow slip events and seismic tremor at circum-pacific subduction zones. *Reviews of Geophysics*, *45*(3), RG3004. https://doi.org/10.1029/2006RG000208

Segall, P., Rubin, A. M., Bradley, A. M., & Rice, J. R. (2010). Dilatant strengthening as a mechanism for slow slip events. *Journal of Geophysical Research*, *115*(B12), B12305. https://doi.org/10.1029/2010JB007449

Selvadurai, P., & Glaser, S. (2017). Asperity generation and its relationship to seismicity on a planar fault: A laboratory simulation. *Geophysical Journal International*, *208*(2), 1009–1025. https://doi.org/10.1093/gji/ggw439

Selvadurai, P. A., & Glaser, S. D. (2015). Laboratory-developed contact models controlling instability on frictional faults. *Journal of Geophysical Research*, *120*(6), 4208–4236. https://doi.org/10.1002/2014JB011690

Sherburn, J., Horstemeyer, M., Bammann, D., & Baumgardner, J. (2011). Application of the Bammann inelasticity internal state variable constitutive model to geological materials. *Geophysical Journal International*, *184*(3), 1023–1036. https://doi.org/10.1111/j.1365-246X.2010.04917.x

Shi, P., Wei, M., & Barbot, S. (2022). Contribution of viscoelastic stress to the synchronization of earthquake cycles on oceanic transform faults. *Journal of Geophysical Research*, *127*(8), e2022JB024069. https://doi.org/10.1029/2022JB024069

Shi, Q., Barbot, S., Shibazaki, B., Matsuzawa, T., Wei, S., & Tapponnier, P. (2020). Structural control and system-level behavior of the seismic cycle at the Nankai trough. *Earth Planets and Space*, *72*(1), 1–31. https://doi.org/10.1186/s40623-020-1145-0

Shibazaki, B., & Shimamoto, T. (2007). Modelling of short-interval silent slip events in deeper subduction interfaces considering the frictional properties at the unstable/stable transition regime. *Geophysical Journal International*, *171*(1), 191–205. https://doi.org/10.1111/j.1365-246x.2007.03434.x

Shimamoto, T. (1986). Transition between frictional slip and ductile flow for halite shear zones at room temperature. *Science*, *231*(4739), 711–714. https://doi.org/10.1126/science.231.4739.71

Shreedharan, S., Ikari, M., Wood, C., Saffer, D., Wallace, L., & Marone, C. (2022). Frictional and lithological controls on shallow slow slip at the northern Hikurangi Margin. *Geochemistry, Geophysics, Geosystems*, *23*(2), e2021GC010107. https://doi.org/10.1029/2021gc010107

Shreedharan, S., Saffer, D., Wallace, L. M., & Williams, C. (2023). Ultralow frictional healing explains recurring slow slip events. *Science*, *379*(6633), 712–717. https://doi.org/10.1126/science.adf49

Sleep, N. H. (1997). Application of a unified rate and state dependent theory to the mechanics of fault zones with strain localization. *Journal of Geophysical Research*, *102*(B2), 2875–2895. https://doi.org/10.1029/96jb03410

Sleep, N. H. (2005). Physical basis of evolution laws for rate and state friction. *Geochemistry, Geophysics, Geosystems*, *6*(11), 720. https://doi.org/10.1029/2005gc000991

Sleep, N. H. (2006). Real contacts and evolution laws for rate and state friction. *Geochemistry, Geophysics, Geosystems*, *7*(8), Q08012. https://doi.org/10.1029/2005GC001187

Stesky, R. (1978a). Rock friction-effect of confining pressure, temperature, and pore pressure. In *Rock friction and earthquake prediction* (pp. 690–704). Springer.

Stesky, R. (1978b). Mechanisms of high temperature frictional sliding in Westerly granite. *Canadian Journal of Earth Sciences*, *15*(3), 361–375. https://doi.org/10.1139/e78-042

Sulem, J., & Famin, V. (2009). Thermal decomposition of carbonates in fault zones: Slip-weakening and temperature-limiting effects. *Journal of Geophysical Research*, *114*(B03309), 14. https://doi.org/10.1029/2008JB006004

Sun, H., & Pec, M. (2021). Nanometric flow and earthquake instability. *Nature Communications*, *12*(1), 6779. https://doi.org/10.1038/s41467-021-26996-0

Tal, Y., Rubino, V., Rosakis, A. J., & Lapusta, N. (2020). Illuminating the physics of dynamic friction through laboratory earthquakes on thrust faults. *Proceedings of the National Academy of Sciences*, *117*(35), 21095–21100. https://doi.org/10.1073/pnas.200459011

Tang, C.-H., Barbot, S., Hsu, Y.-J., & Wu, Y.-M. (2020). Heterogeneous power-law flow with transient creep in southern California following the 2010 El Mayor-Cucapah earthquake. *Journal of Geophysical Research*, *125*(9), e2020JB019740. https://doi.org/10.1029/2020JB019740

Tang, C.-H., Hsu, Y.-J., Barbot, S., Moore, J. D., & Chang, W.-L. (2019). Lower-crustal rheology and thermal gradient in the Taiwan orogenic belt illuminated by the 1999 Chi-Chi earthquake. *Nature Communications*, *5*(2), eaav3287. https://doi.org/10.1126/sciadv.aav3287

Tenthorey, E., & Cox, S. F. (2006). Cohesive strengthening of fault zones during the interseismic period: An experimental study. *Journal of Geophysical Research*, *111*(B9), B09202. https://doi.org/10.1029/2005JB004122

Tenthorey, E., Cox, S. F., & Todd, H. F. (2003). Evolution of strength recovery and permeability during fluid–rock reaction in experimental fault zones. *Earth and Planetary Science Letters*, *206*(1–2), 161–172. https://doi.org/10.1016/S0012-821X(02)01082-8

Terzaghi, K. (1936). The shearing resistance of saturated soils and the angle between the planes of shear. In *International Conference of Soil and foundation engineering* (pp. 54–56). Harvard University Press.

Tian, P., & He, C. (2019). Velocity weakening of simulated augite gouge at hydrothermal conditions: Implications for frictional slip of pyroxene-bearing mafic lower crust. *Journal of Geophysical Research*, *124*(7), 6428–6451. https://doi.org/10.1029/2018JB016456

Tse, S. T., & Rice, J. R. (1986). Crustal earthquake instability in relation to the depth variation of frictional slip properties. *Journal of Geophysical Research*, *91*(B9), 9452–9472. https://doi.org/10.1029/JB091iB09p09452

Tsutsumi, A., & Shimamoto, T. (1997). High-velocity frictional properties of gabbro. *Geophysical Research Letters*, *24*(6), 699–702. https://doi.org/10.1029/97GL00503

Valdez, R., II, Kitajima, H., & Saffer, D. (2019). Effects of temperature on the frictional behavior of material from the Alpine Fault Zone, New Zealand. *Tectonophysics*, *762*, 17–27. https://doi.org/10.1016/j.tecto.2019.04.022

Veedu, D. M., & Barbot, S. (2016). The Parkfield tremors reveal slow and fast ruptures on the same asperity. *Nature*, *532*(7599), 361–365. https://doi.org/10.1038/nature17190

Veedu, D. M., Giorgetti, C., Scuderi, M., Barbot, S., Marone, C., & Collettini, C. (2020). Bifurcations at the stability transition of earthquake faulting. *Geophysical Research Letters*, *47*(19), e2020GL087985. https://doi.org/10.1029/2020GL087985

Verberne, B., Spiers, C., Niemeijer, A., De Bresser, J., De Winter, D., & Plümper, O. (2014). Frictional properties and microstructure of calcite-rich fault gouges sheared at sub-seismic sliding velocities. *Pure and Applied Geophysics*, *171*(10), 2617–2640. https://doi.org/10.1007/s00024-013-0760-0

Wang, B., & Barbot, S. (2023). Pulse-like ruptures, seismic swarms, and tremorgenic slow-slip events with thermally activated friction. *Earth and Planetary Science Letters*, *603*, 117983. https://doi.org/10.1016/j.epsl.2022.117983

Wang, L., & Barbot, S. (2020). Excitation of San Andreas tremors by thermal instabilities below the seismogenic zone. *Science Advances*, *6*(36), eabb2057. https://doi.org/10.1126/sciadv.abb2057

Weber, B., Suhina, T., Brouwer, A., & Bonn, D. (2019). Frictional weakening of slip interfaces. *Science Advances*, *5*(4), eaav7603. https://doi.org/10.1126/sciadv.aav7603

Weeks, J. D. (1993). Constitutive laws for high-velocity frictional sliding and their influence on stress drop during unstable slip. *Journal of Geophysical Research*, *98*(B10), 17637–17648. https://doi.org/10.1029/93JB00356

Wei, S., Helmberger, D., & Avouac, J.-P. (2013). Modeling the 2012 Wharton basin earthquakes off-Sumatra: Complete lithospheric failure. *Journal of Geophysical Research*, *118*(7), 3592–3609. https://doi.org/10.1002/jgrb.50267

Wiederhorn, S. (1967). Influence of water vapor on crack propagation in soda-lime glass. *Journal of the American Ceramic Society*, *50*(8), 407–414. https://doi.org/10.1111/j.1151-2916.1967.tb15145.x

Wintsch, R., Christoffersen, R., & Kronenberg, A. (1995). Fluid-rock reaction weakening of fault zones. *Journal of Geophysical Research*, *100*(B7), 13021–13032. https://doi.org/10.1029/94JB02622

Xing, T., Zhu, W., French, M., & Belzer, B. (2019). Stabilizing effect of high pore fluid pressure on slip behaviors of gouge-bearing faults. *Journal of Geophysical Research*, *124*(9), 9526–9545. https://doi.org/10.1029/2019JB018002

Xu, Y., Scheibert, J., Gadegaard, N., & Mulvihill, D. M. (2022). An asperity-based statistical model for the adhesive friction of elastic nominally flat rough contact interfaces. *Journal of the Mechanics and Physics of Solids*, *164*, 104878. https://doi.org/10.1016/j.jmps.2022.104878

Yamashita, F., Fukuyama, E., & Mizoguchi, K. (2014). Probing the slip-weakening mechanism of earthquakes with electrical conductivity: Rapid transition from asperity contact to gouge comminution. *Geophysical Research Letters*, *41*(2), 341–347. https://doi.org/10.1002/2013gl058671

Yasuhara, H., Marone, C., & Elsworth, D. (2005). Fault zone restrengthening and frictional healing: The role of pressure solution. *Journal of Geophysical Research*, *110*(B6), B06310. https://doi.org/10.1029/2004jb003327

Zeng, L., Chen, Y., Lu, Y., Hossain, M. M., Saeedi, A., & Xie, Q. (2020). Role of brine composition on rock surface energy and its implications for subcritical crack growth in calcite. *Journal of Molecular Liquids*, *303*, 112638. https://doi.org/10.1016/j.molliq.2020.112638

Zhang, F., An, M., Zhang, L., Fang, Y., & Elsworth, D. (2019). The role of mineral composition on the frictional and stability properties of powdered reservoir rocks. *Journal of Geophysical Research*, *124*(2), 1480–1497. https://doi.org/10.1029/2018JB016174

Zhang, L., & He, C. (2016). Frictional properties of phyllosilicate-rich mylonite and conditions for the brittle-ductile transition. *Journal of Geophysical Research*, *121*(4), 3017–3047. https://doi.org/10.1002/2015JB012489

Zhu, W., Allison, K. L., Dunham, E. M., & Yang, Y. (2020). Fault valving and pore pressure evolution in simulations of earthquake sequences and aseismic slip. *Nature Communications*, *11*(1), 1–11. https://doi.org/10.1038/s41467-020-18598-z